1 **Regional groundwater flow dynamics and residence times in Chaudière-**
2 **Appalaches, Québec, Canada: Insights from numerical simulations**
3

4 **D. Janos[1], J. Molson[1,*], R. Lefebvre[2]**
5

6 1 Department of Geology and Geological Engineering, Université Laval,
7   1065, av. de la Médecine, Québec, (QC) G1V 0A6 Canada
8   Tel : 418-656-5713; john.molson@ggl.ulaval.ca

9 2 Centre Eau Terre Environnement,
10   Institut national de la recherche scientifique (INRS-ETE),
11   490, rue de la Couronne, Québec, (QC) G1K 9A9 Canada
12   Tel : 418 654-2651 ; rene.lefebvre@ete.inrs.ca

13
14
15

22
23 *Corresponding author
24 J. Molson: john.molson@ggl.ulaval.ca
25
26

For the use of the editors

Paper #:

Submitted on:

Accepted on:

Application - Research – Commentary – Book Review:

Copyright Held by:

T2012

27

28 **Abstract**

29

30 As part of the Quebec PACES III provincial groundwater resources assessment program, a

31 regional-scale two-dimensional numerical groundwater model was developed in the

32 Chaudière-Appalaches region, Québec, Canada. The model considers groundwater flow,

33 transport of groundwater age and the influence of a fault on the flow system and its

34 implications for groundwater quality. By including deep and shallow flow systems, the

35 study helps fills a knowledge gap with respect to intermediate flow systems and the role

36 they would play during potential energy resource development including shale gas

37 exploitation from the Utica shale. Physical and chemical hydrogeological data, including an

38 analysis of ^{14}C in dissolved inorganic carbon in sampled groundwater, supported a regional

39 conceptual flow model forming the basis for numerical simulations. The model is first

40 calibrated to regional piezometry through a semi-automated workflow using the inverse

41 model PEST. Although some evidence for deeper regional flow exists, the area appears to

42 be dominated by local flow systems on maximum length scales of about 5 km, with

43 significant flow through the top 40 m to 60 m of the fractured sedimentary rock aquifer.

44 This regional-scale flow model is also supported by the local hydrogeochemical signatures.

45 Simulated mean groundwater ages show young shallow water of <100 yrs with rapid

46 increases in age with depth suggesting diffusion-controlled age evolution. Groundwater age

47 is likely being perturbed in the vicinity of a major fault which can act as both a barrier and

48 a preferential pathway, provided permeability contrasts with the surrounding rock are on

49 the order of two orders of magnitude.

50

Résumé

Dans le cadre du projet PACES III pour la région de Chaudière-Appalaches, Québec, au Canada, l'étude présente une analyse approfondie de l'influence des dynamiques d'écoulement sur la qualité des eaux souterraines dans un contexte régional. L'écoulement régional, le transport d'âge et l'impact d'une faille sur la qualité de l'eau souterraine sont étudiés par l'entremise de modèles numériques bidimensionels. En considérant les systèmes d'écoulement profonds et peu profonds, l'étude clarifie les dynamiques intermédiaires qui les relient et le rôle qu'elles pourraient jouer dans l'exploitation potentielle des gaz de shale de l'Utica. La combinaison de connaissances hydrogéologiques physiques et chimiques, y compris une analyse des concentrations de ^{14}C dans les eaux souterraines échantillonnées, a conduit à l'ébauche d'un modèle conceptuel de l'écoulement régional. Le modèle est d'abord calibré à l'aide du logiciel PEST en comparant les charges simulées à la piézométrie régionale. Bien que le modèle affiche l'existence d'un écoulement régional profond, la région à l'étude apparaît être dominée par des systèmes d'écoulements locaux à des échelles maximales d'environ 5 km, avec un écoulement significatif dans le roc fracturé peu profond. L'écoulement actif se limitant à une profondeur maximale de 40 m à 60 m du roc fracturé. La simulation du transport advectif-dispersif de l'âge montre des eaux jeunes de < 100 ans près de la surface et une augmentation rapide de l'âge avec la profondeur suggérant l'importance de la diffusion comme processus de transport. Enfin, les résultats suggèrent que, si le contraste de perméabilité entre la faille et la roche mère est au moins de deux ordres de grandeur, la faille de la Rivière Jacques Cartier pourrait agir comme une barrière ou une zone d'écoulement préférentielle.

Introduction

Understanding relationships between local, intermediate and regional groundwater flow systems (as defined by Tóth, 2009) is critically important for management of water resources as well as to reduce risk of contamination from deep energy resource development (ex. shale gas or geothermal energy). In this context, a regional-scale groundwater research program was initiated in the Chaudière-Appalaches (CA) region, Québec, as part of the groundwater resources assessment program (*Programme d'acquisition des connaissances sur les eaux souterraines*, PACES) of the Quebec Ministry of Environment (*Ministère du Développement durable, de l'Environnement et de la Lutte contre les changements climatiques*, MDDELCC) (MDDELCC 2017). The present study was part of one of many PACES projects, which focused on regional groundwater flow dynamics and natural hydro-geochemistry and geochemical processes in the Chaudière-Appalaches region (Figure 1) (referred to here as PACES-CA).

Figure 1 near here

The Chaudière-Appalaches study area, south of Quebec City, spans over 14,625 km^2 and has a population of approximately 276,000, mainly concentrated near major waterways including the St. Lawrence River, and the Chaudière River and its tributaries (Lefebvre et al. 2015). Although surface water is abundant, almost half of the water usage (42%) in the CA region is extracted from the subsurface.

As groundwater is fundamental to the local economy, groundwater resources within the CA region, both in terms of quantity and quality, have been the focus of a number of studies over the past three decades, culminating in the current PACES project. These projects have helped to characterize the resource, focusing on the most densely populated Chaudière River watershed (McCormack 1982; Rousseau et al. 2004; Benoît et al. 2009; Benoît et al. 2011; Brun Koné 2013; Benoît et al. 2014; Carrier et al. 2014; Lefebvre et al. 2015). Based primarily on data collected from shallow residential wells (with average depths of

4

102   approximately 60 m), these studies have provided important information on groundwater

103   quality and aquifer properties, concluding that groundwater flow occurs primarily within

104   permeable valley sediments and in the top fractured part of the bedrock (< 30 m) (Brun

105   Koné 2013; Benoît et al. 2014; Crow and Ladevèze 2015; Ladevèze et al. 2016; Ladevèze

106   et al. 2017; Ladevèze 2017). Furthermore, Benoît et al. (2014) and Lefebvre et al. (2015)

107   found geochemical signatures left behind by the invasion of the Champlain Sea, which

108   flooded the northern areas of the Chaudière-Appalaches region (Figure 1) about 12,000 to

109   10,000 years ago (Parent and Occhietti 1988).

110   In parallel, the potential exploitation of unconventional gas resources from the Utica Shale

111   of the St. Lawrence Platform geological province, which includes parts of the Chaudière-

112   Appalaches region, led to a series of additional geological and hydrogeological studies led

113   by the Geological Survey of Canada and the INRS (Institut national de la recherche

114   scientifique). These studies aimed to assess the risks of groundwater contamination

115   associated with shale gas exploitation through upward fluid migration and to establish the

116   baseline hydrogeological conditions prior to exploitation. Focusing their case study on the

117   region of Saint-Édouard-de-Lotbinière (Figure 1), Bordeleau et al. (2015) and Rivard et al.

118   (2014) found, despite local flow regimes being more apparent, indications of relatively

119   deep regional flow emerging near the Jacques-Cartier River fault line (Figure 2). Their

120   findings support the conceptualization of regional groundwater flow as a Tóthian flow

121   system (Tóth 1999; Tóth 2009), in which local flow regimes are embedded within larger

122   intermediate or regional flow regimes (Goderniaux et al. 2013). As shale gas exploration

123   areas border the St. Lawrence River (Lavoie et al. 2014; Moritz et al. 2015; Rivard et al.

124   2014), which is a clear outlet for regional groundwater flow, broadening the understanding

125   of how such systems might interact with local flow systems becomes even more important.

126   The aim of the broader PACES-CA study was to reinforce understanding of the regional

127   flow system in the Chaudière-Appalaches region, and included investigating the

128   characteristic time scales of groundwater flow processes through a review of the regional

129   geochemistry and from estimates of groundwater age based on isotopic evidence (Lefebvre

130   et al. 2015). This current paper focuses on testing a conceptual model of the regional

131   hydrogeological system using a two-dimensional numerical flow and age transport model.

132   The numerical modelling aims to quantify the magnitude of regional flow, estimate the

133   maximum depth of active groundwater flow, investigate the distribution of groundwater

134   residence times, and to determine the influence of major normal faults on regional flow.

135

136   *Figure 2 near here*

137

138   **Methodology**

139   The study objectives are met by first carrying out a thorough review of the regional

140   geological context and Quaternary history along with a synthesis of the state of knowledge

141   of the regional geochemistry and an analysis of groundwater ages. Combining the physical

142   and chemical hydrogeological knowledge led to the development of a regional conceptual

143   flow model.

144   The conceptual model was then tested by simulating the regional flow system within a two-

145   dimensional vertical plane, about 70 km long, oriented roughly southeast-northwest from a

146   regional topographic flow divide in the Appalachians towards the St. Lawrence River. All

147   flow simulations are run using the FLONET/TR2 numerical code (Molson and Frind,

148   2017), assuming steady-state, saturated isothermal conditions. The flow model is first

149   calibrated using the PEST inverse calibration model (version 13.6; Doherty 2015). The

150   calibrated flow model and various fault scenarios are then applied in the TR2 transport

151   model to simulate the distribution of groundwater ages. The role of faults is investigated by

152   testing various fault configurations based on the findings of a hydromechanical

153   characterisation of the Saint-Édouard-de-Lotbinière area conducted by Ladevèze (2017)

154   and Bordeleau et al. (2017).

155

156   **Study area**

157   *Geologic and geographic context*

158   Regional landscape and topography is characterized by a combination of various geological

159   settings, dominated by the geological provinces of the Appalachians and the St. Lawrence

160   Platform (Figure 2b). Although both geologic provinces are primarily sedimentary in

161   origin, the Appalachians are highly deformed and slightly metamorphosed whereas the St.

162   Lawrence Platform has undergone almost no deformation.

163   Situated towards the south of the study area, the Appalachians are the remains of a

164   weathered mountain range and are characterised by a hilly terrain. The Appalachian region

165   is marked by granitic intrusions forming small mountains, including the Petits Monts

166   Mégantic and the Monts Notre Dame mountains (Figure 1) reaching elevations up to 850

167   and 1000 m, respectively (Slivitzky and St-Julien 1987). The intrusions are surrounded by a

168   belt of small hills, which are bordered to the south by the Appalachian plateau and to the

169   north by a foothill area that marks the junction with the sedimentary plains of the St.

170   Lawrence Lowlands (Slivitzky and St-Julien 1987). With a history of high tectonic activity,

171   the Appalachian region is marked by the presence of lineaments oriented NE-SW which

172   manifest primarily in the form of major faults (Lefebvre et al. 2015; Caron 2012).

173   In the northernmost part of the study area, the St. Lawrence Platform consists of a

174   sedimentary succession sitting unconformably on the Canadian Shield (Globensky 1987).

175   Due to tectonic compression, normal faults mark the gradual lowering of the sedimentary

176   sequence, which plunges below the Appalachian Basin (Castonguay et al. 2010) as shown

177   in Figure 2b.

178   The Cambrian-Ordovician sedimentary sequence of the St. Lawrence Platform is a typical

179   marine transgression-regression sequence resulting from the opening and closing of the

180   Iapetus Ocean. From bottom up, the sequence begins with the Potsdam Group, a poorly

181   cemented sandstone formation becoming well cemented in its upper portion (Cloutier et al.

182   2006). Above this formation sits the commonly named carbonate platform which is

183   separated into four groups including dolomitic sandstone, dolostone, limestones and shales

184   (Séjourné et al. 2013; Cloutier et al. 2006).

7

185   At depths ranging from 800 to 3000 m, the Utica Shale, which can be considered as marl

186   due to its high carbonate content, has a potential for shale gas production that was tested by

187   vertical and horizontal exploration wells, some of which were subjected to hydraulic

188   fracturing (Séjourné et al. 2013; Lavoie et al. 2014; Bordeleau et al. 2015; Thériault 2012).

189   The overlying Lorraine group, composed of silty shales with mostly non-calcareous

190   sediments interbedded with fine sandstone and clayey siltstones (Thériault 2012) is the top

191   formation of the St. Lawrence Platform sedimentary succession over most of the study area.

192   Many past studies have identified the regional aquifer as being located in the uppermost

193   portion of the bedrock where fracture density is highest (Lefebvre et al. 2015; Benoît et al.

194   2014; Ladevèze et al. 2016). Major faults could also represent areas where the level of

195   fracturing could be relatively high, although the role of these faults on the regional flow

196   system is not clear.

197   Surficial sediments throughout the area are on average 3-5 m deep but can reach 30 m in

198   the valleys. As the study area is generally covered with till deposits of various thicknesses

199   and assemblies, the nature of the till units defines the degree of confinement of the bedrock

200   aquifer. In the Appalachian Highlands, surficial sediments are thin or non-existent,

201   therefore unconfined conditions prevail for most of the fractured bedrock aquifer, with the

202   exception of valleys where the aquifer is generally semi-confined (Lefebvre et al. 2015).

203   Moreover, glaciation-deglaciation processes, the presence of the Champlain Sea

204   approximately 10,000 years ago, and the formation of post-glacial lakes and shorelines, led

205   to heterogeneous deposits with varying proportions of sand and silt. These sediments

206   together with alluvial deposits represent significant infiltration pathways when directly in

207   contact with the bedrock aquifer. On the other hand, scattered silt and clay sediments,

208   deposited at the bottom of stagnant water bodies following glacial retreat, prevent recharge

209   and are responsible for the accumulation of organic material (Lefebvre et al. 2015). These

210   low-permeability deposits are present mostly within the area formerly covered by the

211   Champlain Sea, specifically in the northwestern area of the St. Lawrence Lowlands.

212   Total precipitation over the study area is estimated to be 1149 mm/year, with an average of

213   166 mm/year of recharge reaching the fractured rock aquifer (Lefebvre et al. 2015). Spatial

214   distribution of recharge is highly variable. In the St. Lawrence Lowlands, areas covered

215   with thick layers of fine sediments can receive less than 15 mm/year whereas rock outcrop

216   areas can receive more than 300 mm/year. In the Appalachian Highlands, where the

217   surficial sediments are fairly thin and permeable, aquifer recharge tends to be higher,

218   varying from 100 mm/year to more than 300 mm/year. Additional studies on specific

219   watersheds within the study area have reported overall recharge rates to the bedrock aquifer

220   of between 27 mm/year and 38 mm/year (Benoît et al. 2014 and L'Heureux 2005,

221   respectively). Discrepancies between recharge values could be attributed to its spatial

222   variability.

223

224   *Regional scale conceptual model*

225   Combining the geologic interpretation with the regional piezometric and hydrogeochemical

226   data presented in Lefebvre et al. (2015) led to development of an initial regional conceptual

227   flow and geochemical evolution model (Figure 2a). Most of the groundwater sample data

228   reflected a rapid transit time, thus confirming that flow occurs mostly at shallow depths in

229   the top portion of the fractured rock aquifer where it is under open system conditions with

230   respect to the atmosphere.

231   Based on the analysis of groundwater samples taken from residential wells (Janos 2017),

232   three major water types were found to prevail in the study area, named G1, G2 and G3.

233   First, G1 samples, with typical recharge water geochemical signatures (Ca-HCO$_3$) are

234   found both in the St. Lawrence Lowlands and the Appalachian Highlands (Figure 2a). Most

235   of the samples of this water type were identified as being in an open system with respect to

236   the atmosphere while those in a closed system have the lowest radiocarbon ages found

237   among the three water types. G1 waters would correspond to the active flow layer.

238   In the St. Lawrence Lowlands, the presence of G2 (Na-HCO$_3$)-type waters indicates that

239   salty water which had infiltrated the aquifer during the Champlain Sea invasion has been

240   replaced by fresh water. Above a mean groundwater age threshold of 10,000 years, the

241   salty water twould have been replaced by fresh recharge at least once. Therefore, the waters

242   sampled above this threshold should have a geochemical signature corresponding to G1 or,

243   if cation exchange sites with Na+ ions are present, to G2 water which corresponds to the

244   first step of the freshening process.

245   G3 water types (Na-HCO$_3$/Na-Cl) are related to stagnation zones, long travel paths or

246   mixing with older waters such as formation brines. These water samples have a maximum

247   radiocarbon age of 11,680 Yr B.P., and support the hypothesis that some wells pump from

248   older water horizons. Bordeleau et al. (2017) collected two water samples in the Saint-

249   Édouard-de-Lotbinière area, near the northern end of the study area, at a depth of 48 m

250   below the surface without disturbing the water column in the well, and dated the samples

251   over 1.5 Ma (million years). The work of Vautour et al. (2015) and Saby et al. (2016) also

252   emphasizes the presence of old recharge water and connate brines in near-surface

253   groundwater samples collected in the St. Lawrence Platform.

254   In the St. Lawrence Lowlands, the horizontal hydraulic gradients are lower than in the

255   highlands, thus leading to slower groundwater flow rates, which is reflected in water

256   samples showing signs of water freshening. The presence of such waters in shallow

257   residential wells indicates that the interface between the active flow zone and slow moving

258   groundwater is close to the surface. Furthermore, the presence of waters having old

259   radiocarbon ages, long flow paths and possibly mixing with formation brines from the

260   Appalachians, points to a possible regional flow path emerging near the St. Lawrence

261   River. Overall, the geochemical and isotopic evidence (Lefebvre et al. 2015) suggests that

262   the flow system in the Chaudière-Appalaches region seems to follow the Thóthian regional

263   groundwater flow concept, which is characterised by nested local, intermediate and

264   regional flow systems (Tóth, 2009).

265   Additional insight into developing the 2D conceptual model for this study was provided by

266   a 3D numerical flow model of the Chaudière River watershed (Brun Koné; 2013; Benoît et

267   al. 2015). Using a maximum model depth of 300 m, including shallow unconsolidated

268   sediments and the fractured sedimentary rock, this 3D model showed that most

269   groundwater flow is focussed in the shallow rock. However, the model did not investigate

270   deep regional flow. Additional groundwater flow models in two and three dimensions

271   focusing on flow systems through shallow fractured rock have also been developed for

272   other regions in Québec (Basses-Laurentides: Nastev et al. 2005; Châteauguay: Lavigne et

273   al. 2010; Montérégie Est: Laurencelle et al. 2013; Outaouais: Montcoudiol et al. 2017;

274   Saint-Charles River wastershed: Cochand 2014 and Graf 2015). Although important

275   insight was gained through these studies, the importance and role of deep regional flow in

276   these flow systems remains to be defined.

277

278

279   **Numerical modelling**

280   *Objectives*

281   The numerical model presented herein is specifically aimed at better understanding the
282   relationships between local, intermediate and regional flow systems within the Chaudière-
283   Appalaches region. Furthermore, this study aims at identifying how the main geologic
284   features may influence the behaviour of regional flow. In particular, the study area is
285   marked by the presence of major faults with uncertain hydraulic characteristics and which
286   are presumed to be located within a regional flow discharge zone. A better understanding of
287   the role of faults in regional and deep groundwater flow is particularly important regarding
288   the risk to shallow groundwater quality from potential development of unconventional
289   hydrocarbons (Lefebvre 2017; Rivard et al. 2014).

290   Numerical modelling is used here to investigate the role of these faults on groundwater
291   discharge. While the role of a conduit-type fault has been investigated for a generic
292   regional basin with a geologic context comparable to the St. Lawrence Platform (Gassiat et
293   al. 2013), the hydraulic behaviour of fault zones in the Chaudière study area has yet to be
294   characterised (some early work was presented by Ladevèze et al. 2015 and Ladevèze
295   2017).

296   *Modelling strategy*

297   In order to best capture the dynamics of regional flow in the Chaudière-Appalaches region,
298   a two-dimensional groundwater flow model was developed following a regional flow path
299   (Figure 1), which was then coupled to an advective-dispersive age transport model. The
300   flow and age transport simulations were completed using the finite element FLONET/TR2
301   code (Molson and Frind, 2017).

302   In FLONET/TR2, the two-dimensional steady-state groundwater flow equations are defined
303   as a function of hydraulic heads (Equation 1) and stream functions (Equation 2) (Molson
304   and Frind, 2017):

305    $$\frac{\partial}{\partial x}\left(K_{xx}\frac{\partial \phi}{\partial x}\right) + \frac{\partial}{\partial y}\left(K_{yy}\frac{\partial \phi}{\partial y}\right) = 0 \qquad (1)$$

12

$$\frac{\partial}{\partial x}\left(\frac{1}{K_{yy}}\frac{\partial \psi}{\partial x}\right) + \frac{\partial}{\partial y}\left(\frac{1}{K_{xx}}\frac{\partial \psi}{\partial y}\right) = 0 \qquad\qquad (2)$$

306

307   where x and y are the horizontal and vertical coordinate directions, respectively (L), K_{xx} and

308   K_{yy} are the principal components of the hydraulic conductivity tensor (L/T), φ is the

309   hydraulic head (L), and ψ is the stream function (L^2/T).

310

311   The steady-state saturated flow model was calibrated using PEST version 13.6 (Doherty

312   2015), a model-independent parameter estimation code. Following calibration, a full

313   sensitivity analysis of selected parameters was completed (not shown here; for details see

314   Janos, 2017). The calibrated flow model was then used to simulate the transport of age

315   mass. Finally, a parametric study on the role of faults was performed in order to investigate

316   their potential influence on groundwater flowpaths.

317   ***Domain description***

318   The numerical model domain corresponds to a two-dimensional projection of the geologic

319   cross-section and conceptual groundwater flow model. The model follows an inferred

320   regional flow path which extends from a local peak elevation in the Appalachian Highlands

321   to the St. Lawrence River, being 69 km long with a maximum depth of 9.1 km. Three

322   distinct geological provinces are included in the model: the Grenville crystalline bedrock,

323   relatively flat-lying units of the sedimentary St. Lawrence Platform, and the Appalachians.

324   The entire domain is covered by a discontinuous layer of surficial deposits of marine and

325   glacial or fluvioglacial origin.

326

327   ***Steady-state regional flow model***

328   *Assumptions and limitations*

329   Several assumptions have been made in order to simplify the Chaudière-Appalaches model
330   and reduce over-parameterization. First, given the regional scale of the study, fractured
331   rock is represented as an equivalent porous medium. Also, using a two-dimensional model
332   assumes that groundwater flow is perfectly aligned with the cross-section and thus
333   transverse hydraulic and age gradients are neglected. Since the cross-section is parallel to
334   regional topographic and piezometric gradients, it is considered well representative of the
335   regional flow direction.

336   Furthermore, the flow system is simulated under steady-state conditions and thus does not
337   account for seasonal (or climatic) recharge variations. Transient recharge is expected to
338   have the most impact on local flow systems, with little or no significant impact on regional
339   flow. Furthermore, water table fluctuations induced by seasonal recharge variations are also
340   expected to be negligible with respect to inherent uncertainty, including the errors
341   associated with the extrapolation of the regional potentiometric map, which is assumed to
342   represent an annual average water level. Variations over geological time (ex. ice advances
343   and retreats) are also neglected.

344   Moreover, the model assumes that groundwater in the domain has a uniform temperature,
345   viscosity and density. The average thermal gradient in the area is between 15 and 20 $^{\circ}$C/km
346   (Grasby et al. 2011) which, based on an estimate of the Rayleigh number for average
347   conditions found in the study area, is not sufficient for the onset of thermal convection
348   (Hiscock and Bense 2014). Also, although measured TDS concentrations in the study area
349   reach up to 16,785 mg/L (Bordeleau et al. 2017) and up to 340,000 mg/L in the deep
350   formations of the St. Lawrence Platform (Ngoc et al. 2014), the effects of density and
351   viscosity gradients on flow are assumed less important compared to the 5-6 order of
352   magnitude logarithmic decrease with depth of the hydraulic conductivities (discussed later).

353

14

354 *Domain extent and discretization*

355 The initial top boundary elevations of the model, representing the water table, were

356 extracted from the regional potentiometric map (Lefebvre et al. 2015), while the elevations

357 of the bedrock interface and the nine distinct surficial deposit layers were obtained from a

358 detailed cross-section of surficial deposits traced roughly along the modeled section

359 (Lefebvre et al. 2015). For modelling purposes, the rock formations within the cross-

360 section were divided into five different zones representing different rock types: the St.

361 Lawrence Platform, the Appalachian Highlands, the Utica shale, the carbonate platform and

362 silicate bedrock of the Grenville Province.

363 The finite element flow model is discretized using linear triangular elements with a

364 horizontal discretization of 50 m and a vertical discretization between 0.1 and 50 m

365 (increasing from top to bottom), for a total of 358,000 nodes and 797,640 elements.

366 **Material properties**

367 Material properties represented by the model can be classified as surficial deposits, the

368 fractured bedrock aquifer and deep units.

369 *Surficial deposits*

370 Surficial deposits along the cross-section are composed of nine different hydrostratigraphic

371 units (Lefebvre et al. 2015): organic deposits, alluvium, lakeshore delta sediments,

372 glaciomarine delta deposits, coarse and fine-grained littoral glaciomarine deposits, fluvio-

373 glacial deposits, till and undifferentiated sand. Each unit is represented by a layer of

374 deformed elements in the model (Table 1). All layers of the surficial deposits were assumed

375 to have an average porosity of 0.3.

376 Till is the most prominent unit over the study area and it is thus expected that its hydraulic

377 conductivity will control groundwater recharge into the fractured rock aquifer. The till unit

378 also has the most heterogeneous composition; typically very sandy in the area of the cross-

379 section, its texture can vary abruptly from a permeable sand facies with a few pebbles to an

380 essentially impermeable stony and clayey silt (G. Légaré Couture, personal communication

381 2013). Uncertainty with respect to the hydraulic conductivity of the till layer was addressed

382 through calibration and sensitivity analysis (Janos, 2017).

383 *Fractured bedrock*

384 Hydraulic conductivities of the bedrock were obtained through the updated PACES-

385 Chaudière-Appalaches database (Lefebvre et al. 2015) from which the extensive public

386 well drillers' log data were used to estimate hydraulic conductivities (Figure 3). These data

387 originate from specific capacity data while accounting for drilling and testing biases (M.

388 Laurencelle, personal communication, June-July 2015; Lefebvre et al. 2015). Calculated

389 hydraulic conductivities in the shallow bedrock (within the top 100 m of the rock surface)

390 are between 3.8×10^{-10} and 6.5×10^{-4} m/s in the St. Lawrence Platform (241 data points) and

391 between 5.2×10^{-12} and 3.8×10^{-3} m/s in the Appalachian Highlands (4966 data points).

392 Although the hydraulic conductivity of the bedrock is highly variable for a given depth,

393 spanning more than 6 orders of magnitude, a clear trend of decreasing hydraulic

394 conductivity with depth can be observed for both geologic provinces (Figure 3) (Lefebvre

395 et al. 2015). The calibrated hydraulic conductivities were obtained by adjusting the

396 parameters of an exponential decay function given by Equation 3:

397 $$\log[(K(z)] = log[K_{min}] - (log[K_{max}] - log[K_{min}])e^{-\alpha z} \tag{3}$$

398 where z (m) is the depth below the top of the bedrock surface, K(z) is the hydraulic

399 conductivity at depth z, K_{min} is the minimum hydraulic conductivity asymptotically

400 approached by the curve, K_{max} is the maximum hydraulic conductivity, and α is a curve

401 decay constant (values given in Figure 3).

402

403 **Figure 3 near here**

404

405 *Deep layers*

406 The Grenville basement rock, the St. Lawrence Carbonate platform and the Utica Shale are

407 described in the literature as having distinct hydraulic properties (Table 2). In the model,

408 these units are differentiated from the top fractured unit of the St. Lawrence Platform

16

409 (Lorraine formation) and the Appalachian Highland formations. Conductivities assigned to

410 these deep formations are described in Table 2.

411

412 *Flow boundary conditions*

413 Vertical boundaries, corresponding to the St. Lawrence River to the north-west (left

414 boundary) and to a regional topographic and piezometric peak to the south-east (right

415 boundary), are assumed to represent symmetric physical boundaries of the flow system and

416 were thus assigned a no-flow boundary condition (Figure 4). It is also assumed that no

417 significant flow occurs below a depth of 9,100 m, thus a zero-flux condition was applied to

418 the base of the model. At stream and river locations, the top boundary is constrained by

419 imposed heads. Given that recharge is highly variable over the study area, the top boundary

420 was separated into 295 sections; each with a unique recharge imposed as a Type-2 flux

421 boundary condition which was determined with PEST during calibration. At these recharge

422 locations, the water table elevations were determined iteratively through vertical grid

423 deformation (maximum of 10 layers) until the computed water table head equalled its

424 elevation within a tolerance of 10^{-4} m (Molson and Frind, 2017).

425

426 *Figure 4 near here*

427

428

429 *Flow model calibration*

430 The numerical flow model was calibrated through a semi-automated workflow using PEST

431 (version 13.6, Doherty 2015). PEST is a model-independent parameter estimation code

432 which uses the Gauss-Levenberg-Marquardt search algorithm (GLMA) to minimize the

433 difference between a set of observed (known) values and the corresponding simulated

434 results (Doherty 2015). This software can be particularly useful when a large number of

435 parameters need to be adjusted (calibrated) and when the relationship between the

17

436   parameters and the observations is not linear (eg: Siade et al. 2015; Hayley et al. 2014; Zhu

437   et al. 2015). Nevertheless, when field observations are not sufficient to appropriately

438   constrain a model, calibration solutions will be non-unique and human input is needed to

439   identify the most plausible solution. To this effect, PEST was used in this project to create

440   many realisations of the flow model, each constraining the parameters of the model

441   differently through various iterations of the parameter estimation. The realisation with the

442   best fit to observations and with the most plausible parameters was selected as the base case

443   calibrated model.

444   Calibration was completed by coupling PEST to FLONET and allowing PEST (1) to

445   modify the hydraulic conductivities of each surficial deposit layer, (2) to define the

446   decrease in hydraulic conductivity in the fractured bedrock using Equation 3, and (3) to

447   vary the imposed Type-2 Neumann surface recharge boundary conditions. Given the spatial

448   variability in recharge calculated from one-dimensional infiltration models (Lefebvre et al.

449   2015; Benoît et al. 2014), recharge values imposed along the top boundary of the model

450   were allowed to vary between 0 and 900 mm/year.

451   The observations, to which PEST was trying to find the best fit, were taken to be the

452   elevation of the water table at each of the top boundary nodes, and were extrapolated from

453   a regional potentiometric map based on 15,790 observation wells throughout the basin

454   (Lefebvre et al. 2015). Because these data were collected over several decades and at

455   different times of the year, they are considered an accurate long-term representation of the

456   water table and are consistent with the steady-state assumption in the model. The average

457   recharge values imposed on the model by PEST were verified to be consistent with the

458   values calculated from the one-dimensional infiltration model, HELP (Lefebvre et al. 2015;

459   Benoît et al. 2014), based on the approach of Croteau et al. (2010).

460   With respect to the observed heads, which in the study area vary between 0 and over 600

461   m, the final calibrated model heads have an absolute mean error of 2.06 m, a root mean

462   square error (RMSE) of 3.28 m and a maximum absolute error of 18.26 m (Figure 5). The

463   error on simulated heads is well below 5% of the overall variations in heads in the model

464   domain (30 m), which according to Anderson and Woessner (1992) defines the

465   acceptability of a groundwater model hydraulic head calibration. A longitudinal profile

466   comparing the observed and simulated heads, together with surface topography and

467   recharge, is provided in Figure 6.

468   The average overall calibrated recharge to the bedrock is within 1.04% of the average

469   recharge estimated with the HELP model (Table 3; Figure 6). Despite some regional

470   differences between the model-calibrated average recharge to bedrock and the average

471   values calculated with HELP, these calibrated recharge rates remain within the range of

472   values estimated with HELP (Table 3). The model can therefore be considered as a fair

473   representation of the natural groundwater system at the regional scale.

474   Calibrated hydraulic conductivities of the surficial deposits are within limits found in the

475   literature, with the exception of the till layer having a calibrated hydraulic conductivity

476   slightly higher than reported (Table 1). The same trend is observed in the calibrated

477   hydraulic conductivity distribution of the fractured bedrock (Figure 3),which is an order

478   magnitude higher than the median hydraulic conductivities inferred from the well drillers'

479   log data.

480   This discrepancy between measured and calibrated hydraulic conductivities can be

481   attributed to the well-documented scaling effect (Schulze-Makuch et al. 1999; Zhang et al.

482   2006; Nastev et al. 2004). The smaller the measurement volume of a hydraulic test

483   performed in an aquifer, the less likely it is to intercept a preferential flow pathway such as

484   a high-K channel or interconnected fractures. Schulze-Makuch et al. (1999) observed that

485   upscaling the radius of influence of hydraulic testing in a given heterogeneous aquifer

486   could lead to an increase in measured hydraulic conductivity of up to one order of

487   magnitude. This scale effect was also observed for fractured rock aquifers of the St.

488   Lawrence Platform (Nastev et al. 2004).

489   In this study, hydraulic conductivities of the fractured bedrock (Figure 3) were mostly

490   obtained from specific capacity tests for residential wells, which have a relatively small

491   radius of influence of approximately 20 m (Nastev et al. 2004). Lefebvre et al. (2015)

492   describe heterogeneities within the tills of the Chaudière-Appalaches region which would

493   lead to similar scale effects of hydraulic conductivity measurements.

494

19

495   *Figure 5 near here*

496   *Figure 6 near here*

497

498   *Flow model results*

499   Figures 7 and 8 show the simulated potentiometric field and streamlines (flow lines) of the
500   calibrated groundwater flow model, which shows evidence of a Tóthian flow pattern with
501   embedded regional, intermediate and local flow systems (Tóth 1999; Tóth 2009).

502   The simulated flow system is consistent with previous studies (Brun Koné 2013; Benoît et
503   al. 2014) which suggested a dominance of local groundwater flow systems, mostly
504   concentrated in the permeable sediments and within the top 20 to 40 m of the fractured
505   bedrock aquifer. Although the simulated local flow systems in the Appalachian Highlands
506   extend in some areas down to 800 m below the bedrock surface (Figure 7 and 8a), the
507   relative significance of the volume of flow decreases rapidly with depth. These local flow
508   systems have a maximum horizontal scale of approximately 5 km.

509   In this study, active flow is defined as being in those areas which receive an average
510   groundwater flux of more than 1 mm/year, which is reached at a depth of approximately 30
511   m below the rock surface in the St. Lawrence Lowlands and approximately 60 m below the
512   rock surface in the Appalachian Highlands (Janos 2017). The difference in the depth of the
513   active flow zone between these two geological provinces highlights the effects of
514   topography and recharge on the shape of the flow systems.

515   Furthermore, the prominent topographic features of the Appalachian Highlands also
516   generate an intermediate flow system originating from the highest topographic peaks to the
517   south and emerging at the Appalachian foothills, spanning more than 20 km (Figures 7 and
518   8a).

519   Under the assumed simulated conditions, the model also suggests the presence of a deep
520   regional groundwater flow path which originates from the Appalachian Highlands and
521   emerges near the St. Lawrence River (Figure 7). However, this regional system (defined

20

522   between the two deepest streamlines in Figure 7), containing only about 0.5 m^3/year per

523   meter of transverse width, represents less than 0.005% of the total flow in the domain.

524   Mean groundwater age simulations presented later also show that this deep flow would be

525   extremely slow, with mean ages on the scale of geological time (tens of millions of years).

526   A sensitivity analysis (not shown; see Janos, 2017) showed that the regional flow system is

527   relatively insensitive to variations in the hydraulic conductivity of the surficial deposits,

528   while in the Appalachian Highlands, the depth of active flow seemed very sensitive to the

529   hydraulic conductivity of the bedrock and to recharge variations. Deep intermediate and

530   regional flow was highly affected by the bedrock hydraulic conductivity and to a lesser

531   degree by the imposed recharge.

532   ***Figure 7 near here***

533   ***Figure 8 near here***

534

535

536 **Groundwater age simulations**

537 *Modelling approach*

538 In addition to using groundwater flownets, simulated mean groundwater ages can also be

539 useful for interpreting flow systems. Groundwater age is defined as the time elapsed since

540 water entered the groundwater system (Kazemi et al. 2006; Goode 1996).

541 In the TR2 groundwater model, mean groundwater age is taken to be the average (mean)

542 age of a packet of water molecules at a given point in space (Molson and Frind 2017;

543 Bethke and Johnson 2008), and is calculated using Goode's (1996) method for direct

544 simulation of groundwater age. The approach is more realistic than kinetic, or advective

545 age, since it allows age mixing (dispersion) by applying the advection-dispersion transport

546 equation (Equation 4; see also Molson and Frind 2012):

547
$$\frac{\partial}{\partial x_i}\left(D_{i,j}\frac{\partial A}{\partial x_j}\right) - v\frac{\partial A}{\partial x_i} + 1 = 0 \tag{4}$$

548 where A is the mean age (T), D_{ij} is the hydrodynamic dispersion tensor (L^2/T), v is the

549 groundwater velocity (L/T), and the term +1 represents the age growth factor (1 day/day).

550 Janos (2017) compares these advective-dispersive ages with particle-track based advective

551 ages, and with measured ^{14}C ages.

552 *Transport model boundary conditions and parameters*

553 The calibrated steady-state groundwater flow model was used as the base velocity field to

554 simulate mean groundwater ages within the 2D cross-section of the Chaudière-Appalaches

555 regional model. A finite element mesh identical to the flow model was used in the age

556 transport model.

557 In the age transport model, lateral and bottom boundaries are set as zero age-mass gradient

558 Type-2 (Neumann) boundaries. Those sections of the top water table surface which act as

559 inflow recharge boundaries are set as a Type-1 (Dirichlet) boundary condition with a fixed

560 age of A=0 days. Surface nodes acting as discharge points, i.e. nodes connected to elements

561 with an outward pointing velocity vector, are applied a zero-gradient age boundary

22

562   condition. A growth rate of +1 day/day ensures the aging of water as the simulation

563   progresses over time until steady-state is reached between the constant ageing of water and

564   rejuvenation from younger recharge water.

565   The dispersion tensor D_{ij} in Equation 4 is defined using the Lichtner formulation (Lichtner

566   et al. 2002) which has four dispersivity components: two longitudinal (α_{LH} and α_{LV}) and

567   two transverse dispersivities (α_{TH} and α_{TV}). Based on scaling relationships of Xu and

568   Eckstein (1995) and Schulze-Makuch (2005), the longitudinal horizontal dispersivity of the

569   current transport model was set to 50 m. The longitudinal vertical dispersivity (α_{LV}) was set

570   to 10 m, while the two transverse dispersivities were set to 0.05 m. The molecular diffusion

571   coefficient was 1×10^{-10} m^2/s, similar to a conservative tracer. Similar dispersion and

572   diffusion terms were applied in 2D and 3D age transport modelling by Montcoudiol et al.

573   (2017) and Molson and Frind (2012).

574   The Peclet accuracy criterion, which constrains the spatial discretization by limiting the

575   ratio of advection to dispersion (Molson and Frind, 2017), is respected throughout most of

576   the domain. Using adaptive time-stepping, the Courant stability criterion (Molson and Frind

577   2017) is also generally respected for all time steps. Since the steady-state age simulations

578   showed good convergence and relatively minor numerical oscillations, the spatial and

579   temporal discretization was considered acceptable.

580   *Mean groundwater age distribution*

581   The advective-dispersive groundwater age simulation reached steady state at 47.5 Ma for

582   the base case scenario (Figures 9 and 10), which corresponds to the maximum simulated

583   groundwater residence times in the Grenville basement rock. The nested flow systems

584   create a unique mean age distribution which is organized into a complex pattern.

585   The active flow layer within the local flow systems is characterised by short residence

586   times, with mean groundwater ages being generally less than 100 years (Figures 9 and 10).

587   Interestingly, the age simulation shows that the depth of the local flow systems extends

588   well below the active flow layer. The maximum mean age of groundwater in these local

589   flow systems is about 100,000 years (Figure 10 a, b and c). While numerous ground surface

590   discharge zones maintain relatively young ages within these shallow flow systems, mean

23

591   ages nevertheless increase exponentially with depth which is attributed to the exponential

592   decrease in the bedrock hydraulic conductivity, and to the natural distribution of regional

593   flow, as shown by Vogel (1967) for simple single-compartment homogeneous systems with

594   a single discharge zone. Goderniaux et al. (2013) presented similar behavior in numerical

595   simulations of nested flow systems.

596   Furthermore, while the presence of an intermediate flow system in the Appalachian

597   Highlands was clear from the flow simulation, the simulated mean groundwater ages also

598   suggested the existence of such a system with a similar age distribution in the St. Lawrence

599   Lowlands, between about 15 and 30 km along the section (Figure 9).

600   However, contrary to the Appalachian Highlands, in the St. Lawrence Lowlands the age

601   distribution is marked by an abrupt transition between the regional and the smaller scale

602   flow systems. In some portions of the cross-section, for example, the mean age gradient

603   spans two orders of magnitude over very short vertical spatial scales on the order of 50 to

604   100 m (Figure 10b and 10c). Numerous sharp vertical 'plumes' of older water also appear

605   along the profile where deep flow is discharging to surface water (Figure 10). As it reaches

606   the high permeability shallow aquifers, this older water is rapidly diluted by faster flowing

607   young water. This behaviour is consistent with Zijl's (1999) observation that in real steady-

608   state flow systems, mixing zones between transport systems are relatively thin, and thus the

609   interface is generally sharp between water bodies with different water qualities (or ages)

610   which belong to different flow systems. Where the age interface is horizontal, vertical

611   diffusive age mixing prevails.

612   On a regional scale, the average residence times in the deep flow system gradually increase

613   toward the discharge area (Figure 9). Regional flow in the St. Lawrence Lowlands seems to

614   follow a deep preferential pathway through the carbonate platform before emerging near

615   the St. Lawrence River. This flow pattern and age distribution is due to the difference in the

616   assigned hydraulic conductivities between the Lorraine formation, the Carbonate platform

617   and the Utica Shale. Among these three units, the Carbonate platform was assigned the

618   highest hydraulic conductivity while the Utica shale was assigned the lowest, creating a

619   hydraulically isolated permeable unit in which water could travel faster than in the

620   overlying and underlying geologic units. Slower flow above the carbonate platform results

24

621   in an inverted distribution of groundwater residence times where older groundwater in the

622   shale can be found above younger water in the carbonates (Figure 9).

623   *Figure 9, 10 near here*

624

625   **Parametric study on faults**

626   The Utica Shale formation (Figure 4), was recently targeted by the oil and gas industry as

627   an unconventional natural gas reservoir. Public debate surrounding the environmental risks

628   associated with such exploitation has raised many questions with respect to possible aquifer

629   contamination (Rivard et al. 2014; Lavoie et al. 2014; Lefebvre 2017; CCA 2014).

630   While surface releases of fluids related to unconventional oil and gas operations (Vengosh

631   et al. 2014) and well integrity (Roy et al. 2016; Nowamooz et al. 2015) pose the greatest

632   threat to aquifers, geochemical evidence also seems to point to instances in which deep-

633   seated fluids have migrated to the surface along natural preferential flow pathways, such as

634   faults (Révész et al. 2010; Warner et al. 2012). Yet, much debate still exists surrounding the

635   possibility of shallow aquifer contamination through such pathways (Lefebvre 2017).

636   While the question is often viewed from the perspective of the impact of fracking on fluid

637   migration (Gassiat et al. 2013; Flewelling and Sharma 2014; Birdsell et al. 2015; Lange et

638   al. 2013; Kissinger et al. 2013), natural mechanisms, such as regional flow which can

639   contribute to the upward migration of natural formation fluids prior to exploitation, is less

640   often explored.

641   Based on the observation of saline waters in valleys, Warner et al. (2012) hypothesised that

642   the combination of high hydrodynamic pressure at depth under discharge areas (from

643   regional flow for instance) and the presence of higher permeability fracture zones can

644   induce steep hydraulic gradients which could lead to migration of fluids between deeper

645   strata and the surface. Indeed, this phenomenon seems to be occurring in our study area.

646   Based on methane concentration observations, Pinti et al. (2013) suggested that the

647   Yamaska Fault, an extension of the Jacques-Cartier River Fault (Figure 2), could act as a

648   connection between deep formations and surface aquifers. Moreover, focusing their

25

649 research on the Lotbinère study area, located at the northern end of the modeled cross-
650 section (Figure 2), Lavoie and al. (2016) and Bordeleau et al. (2017) also found
651 geochemical and physical evidence of upward flow near the Jacques Cartier River Fault,
652 suggesting that it could act as a preferential pathway for migration of deep groundwater.

653 In this section, the potential role of a fault zone in a regional groundwater discharge area
654 will be investigated through further numerical simulations. Since data gaps exist in the
655 physical characterization of the deep subsurface in the study area, this analysis does not
656 attempt to deliver a definitive interpretation of the flow dynamics occurring near the
657 Jacques-Cartier River Fault. The intent is rather to explore what impact different fault
658 configurations would have on the hydraulic gradients and the distribution of mean
659 groundwater ages near the fault zone as a basis for further studies.

660 ***Modeled fault configurations***

661 In the context of this study, the fault zone is considered to be the volume of rock where the
662 permeability has been altered as a result of fault-related deformations, while the protolith is
663 considered the undeformed rock surrounding the fault zone (Bense et al. 2013). Resulting
664 from tectonic activity, fault zones are complex hydraulic structures with various degrees of
665 deformation. The fault core (FC) generally refers to the central zone of the fault which has
666 undergone the most intense strain and most of the displacement, and as a result can have a
667 lower permeability than the protolith (Bense et al. 2013). On the other hand, the damage
668 zone (DZ), surrounding the fault core, is defined as the region which absorbed the
669 remaining strain and as a result is marked by fracturing and an enhanced permeability
670 (Bense et al. 2013).

671 The degree and nature of the rock deformation attributed to faulting depends on many
672 intrinsic controls such as lithology, fault displacement and geometry, and deformation
673 conditions (Caine et al. 1996) which are difficult to characterize. Furthermore, the
674 definition of the fault's permeability structure has also been shown to depend on the
675 observation methods and geoscience discipline (Scibek et al. 2016).

676 Large-scale fault structures are often segmented and complex, exhibiting multiple fault
677 cores and overlapping damage zones (Bense et al. 2013). In the current study, for the sake

26

678 of simplicity and based on the conceptual model of Ladevèze (2017) proposed for the study

679 area, the permeability structure of the Jacques-Cartier River fault zone is represented by a

680 simplified conduit-barrier-conduit model (Figure 11). This model assumes the fault core is

681 less permeable and the damage zone more permeable than the protolith.

682 *Figure 11 near here*

683 A number of fault characteristics such as the dip, the thickness and permeabilities of the

684 fault zone and those of its core and its damage zone can play a role in controlling fluid flow

685 around a fault (Bense et al. 2013). This study will focus on the impact of the permeability

686 contrasts between the different parts of the fault zone by simulating a range of fault

687 permeability structures (Table 4). Since the scale and nature of the hydrogeological

688 numerical model herein is not suited for representing discrete fractures, the damage zone

689 and fault core are represented using equivalent porous media. The geometry and dip of the

690 fault are based on the geologic cross-section of Séjourné et al. (2013) (Figures 2 and 11)

691 extending from the bedrock surface to the top of the crystalline formation of the Grenville

692 Province. The thicknesses of the modeled fault core and the two damage zones each

693 corresponds to the width of one numerical grid element (50 m). For the different scenarios,

694 the horizontal and vertical hydraulic conductivities of the fault core and damage zones are

695 increased or decreased by up to three orders of magnitude with respect to the laterally

696 adjacent elements corresponding to the protolith (Table 4), while retaining their original

697 anisotropy. As the hydraulic conductivity of the Lorraine Group decreases with depth, so

698 does that of the fault zone where it crosses the Lorraine Group. For comparison, tested

699 scenarios also include conduit-only and barrier-only fault types.

700 *Fault model results: Groundwater flow and age*

701 Flow and age transport results for the various fault scenarios (Figures 12 and 13; see also

702 Figures C1 to C4 in Annex C of Janos, 2017) show that in the simulated flow system a

703 hydraulic conductivity contrast of at least two orders of magnitude between the protolith

704 and the fault zone is required to induce significant diversion of the regional flow system. If

705 the fault is acting as a barrier only, effects of the fault on the flow system begin to be

706 observable when the fault zone hydraulic conductivity is two orders of magnitude less than

27

707 that of the protolith but becomes truly significant with a three order of magnitude

708 difference. Conversely, when the fault is acting as a conduit only, flow diversion is

709 observable with only one order of magnitude difference in hydraulic conductivities between

710 the fault and the protolith and, with a two order magnitude difference, the conduit

711 behaviour of the fault becomes clearly evident. This indicates that in the simulated system,

712 the higher K of the damage zone exerts a greater influence on the flow system than the low

713 K fault core (Figure 12).

714 From an age transport perspective (Figure 13), the presence of an effective barrier, that is a

715 fault core with a hydraulic conductivity of at least 3 orders of magnitude lower than that of

716 the protolith, has the effect of lowering the active flow interface and decreasing the mean

717 ground water ages downstream of the fault (Figure 13-D). By blocking regional flow, the

718 barrier fault isolates the downstream flow system and local flow can penetrate deeper.

719 Interestingly, an effective conduit-type fault, with a hydraulic conductivity at least two

720 orders of magnitude higher that the protolith, has a dual effect on the distribution of mean

721 groundwater ages. For the regional flow system, the conduit-type fault zone is an effective

722 preferential pathway, through which old water originating from long regional flow paths is

723 concentrated and which may reach the surface (Figure 13: I and M). However, in terms of

724 the local flow system, the conduit-type fault also behaves somewhat as a drain, drawing

725 water into the fault zone and thereby decreasing the mean groundwater ages and lowering

726 the active flow interface upstream of the fault. This has the effect of displacing the old

727 water plume from upstream to downstream of the fault (Figure 13: I and M).

728 Combining a barrier-type fault core flanked with a conduit-type damage zone emphasizes

729 the effects of both the barrier and conduit zones (Figure 13: P). On the upstream side of the

730 fault zone, the damage zone channels regional flow which is then effectively blocked by the

731 fault core, allowing the plume of older water to reach closer to the surface before mixing

732 with the local system. On the downstream side of the fault, the damage zone acts as a

733 channel for local flow, allowing recharge to penetrate deeper into the subsurface and

734 creating a larger mixing zone.

735 The most important outcome from this parametric study is that in the regional discharge

736 area, the presence of a fault with a damage zone and/or a fault core with a significantly

28

737   contrasting hydraulic conductivity with the protolith has the potential to divert and channel
738   regional flow similar to a preferential pathway.

739   Nonetheless, this study represents a simplified model of the Jacques-Cartier fault and
740   should only be viewed as a basis for further fault zone characterizations. To more
741   accurately assess the impact of the Jacques-Cartier fault on the emergence of regional flow
742   and its potential to act a pathway for contaminants related to fracking activities, further
743   modelling should be performed taking into account the full complexity of fault zone
744   hydrogeology. Such a model should refine the definition of the permeability structure of the
745   fault zone and consider additional hydrodynamic processes which are relevant to deep basin
746   flow such as density-dependent flow, pressure gradients in deep formations and multiphase
747   flow.

748   *Figures 12, 13 near here*

749

750   **Discussion**

751   The aim of this study was to reinforce understanding of regional flow dynamics in the
752   Chaudière-Appalaches region through the analysis of characteristic time scales using
753   geochemistry and numerical modelling. The conceptual model is based on Tóth's (1999)
754   topography-driven flow model and outlines the presence of local, intermediate and
755   regional-scale flow systems.

756   The main regional aquifer was reported to be located in the upper fractured bedrock
757   (Lefebvre et al. 2015; Benoît et al. 2014; Brun Koné 2013) and the numerical modelling
758   presented herein confirms that the logarithmically decreasing hydraulic conductivity of the
759   bedrock maintains active flow of groundwater in the top 40 m of the fractured rock. While
760   simulated mean groundwater ages in the active flow zones are generally less than 100
761   years, travel times through the deeper local flow systems can reach more than 1 Ma. The
762   slightly shallower active and local flow systems in the St. Lawrence Lowlands with respect
763   to the Appalachian Highlands, highlights the effect of topographic relief on the local flow
764   systems.

765 Rapid increases of the simulated mean groundwater ages with depth in the local flow

766 systems appear to match the conceptual geochemical distribution model of the different

767 water types (Figure 2). Water drawn from residential wells, which extend on average to

768 depths of 60 m, would include young (G1-type) water from the active flow zone where

769 flow rates are fastest, but would in some cases also include water from below the active

770 flow zone - yielding the maximum radiocarbon age of 3500 yr B.P observed in this water

771 group (Janos 2017). Furthermore, local flow systems in the study area can extend to

772 maximum depths of approximately 200 m, and are likely affected by upward diffusion of

773 old water from the regional flow system. A water composition gradient can therefore be

774 expected within the same local flow system.

775 Moreover, the depth of 60 m in the model also roughly matches the zone where mean

776 groundwater ages correspond to the retreat of the Champlain Sea. Water drawn from

777 residential wells below the 10,000 year threshold will most likely be a mixture of salty

778 water from the invasion episode and water that has recharged within the local flow system

779 before the invasion. Given the relatively shallow local flow systems, in many cases it would

780 also be highly probable for a residential well to intercept an intermediate or even the

781 regional flow system.

782 Residential wells, however, are often installed as open boreholes in the bedrock aquifer and

783 thus the water they yield is a mixture of the different geochemical layers they cross. As

784 shown by the flow model, groundwater flow velocities decrease drastically with depth, thus

785 contributions from the deeper layers of local flow systems and those of the regional system

786 are expected to be less significant than those of the active flow layer.

787 The two water samples dated at 1.5 Ma by Bordeleau et al. (2017) were collected from a

788 relatively shallow depth of 48 m near regional fault lines suggesting regional faults such as

789 the Jacques-Cartier River fault could act as preferential discharge pathways for regional

790 flow. The parametric modelling study on fault zone permeability distributions showed that

791 several orders of magnitude difference in hydraulic conductivities between the protolith, the

792 damage zone and the fault core is required for the conduit/barrier effect of the fault to be

793 significant. However, modelling also demonstrated that fault zones can indeed concentrate

794 the input of regional flow to the active flow zone. Regional flow in Chaudière-Appalaches

795　is almost insignificant with respect to the active flow system and is therefore difficult to
796　identify in the field. However, large-scale heterogeneities such as faults which have the
797　effect of concentrating flow, can enhance the detectability of regional flow in near-surface
798　groundwater samples.

799

800　**Conclusions**

801　As part the PACES aquifer characterization program, the conceptual and numerical flow
802　and age transport models presented herein aimed to reinforce understanding of the regional
803　flow system in the Chaudière-Appalaches region.

804　Based on a review of the regional geochemical context and the interpretation of
805　radiocarbon ages of groundwater samples collected in the study area, groundwater flow was
806　conceptualized as a nested flow system dominated by a series of shallow local flow
807　systems. The 2D numerical groundwater flow model developed along a theoretical flow
808　path confirms the presence of nested local, intermediate and regional flow systems.

809　Simulations of groundwater flow and age transport add to the evidence that groundwater
810　flow in the Chaudière-Appalaches region is mainly focused in the uppermost portion of the
811　bedrock (< 40m) where the fracture density is the highest, and suggest that near-surface
812　fractures play an important role in controlling the flow. Below the active flow zone, mean
813　groundwater ages in the local flow systems increase exponentially with depth. The effect of
814　topography on the flow system is dominant in the Appalachian Highlands, which has well-
815　developed intermediate flow systems. On the other hand, intermediate flow systems in the
816　St. Lawrence Lowlands are almost non-existent and the interface between local and
817　regional flow is relatively shallow (40-60 m).

818　While the fractured bedrock in the study area is well characterized near the surface
819　(Lefebvre et al. 2015; Crow and Ladevèze 2015; Ladevèze et al. 2016; Ladevèze et al.
820　2017), there is also evidence that major faults in the study area could likewise be associated
821　with areas at a greater depth where the level of fracturing would be higher (Pinti et al. 2013;
822　Lavoie et al. 2016; Bordeleau et al. 2017). Parametric modelling of a series of fault zone

31

823 permeability distributions showed that a conduit, barrier or conduit-barrier-conduit-type

824 fault could indeed act as a preferential pathway to regional groundwater flow and could

825 explain the occurrence of geochemically evolved and old groundwater near such structures.

826 While the flow and mean age transport numerical model was useful for interpreting the

827 general behaviour of the flow system, important simplifications were made due to data

828 gaps. Additional field work focusing on better characterizing the permeability structure

829 near the Jacques-Cartier River Fault and the vertical distribution of groundwater salinity

830 and mean age could help validate the presented conceptual model and provide further

831 insight into the role of fault zones located in regional discharge areas. Further modelling,

832 incorporating a variable density distribution and a transient flow system would also deepen

833 the understanding of the Chaudière-Appalaches regional flow dynamics.

834

835 **Ackowledgements**

848
849

850

References

Anderson, M.P., and W.W. Woessner. 1992. *Applied Groundwater Modeling*. San Diego: Academic Press, 381 p.

Appelo, C.A.J., and D. Postma. 2005. *Geochemistry, Groundwater and Pollution*. 2nd Edition, Leiden: Balkema, 649p.

Beaudry C. 2013. Hydrogéochimie de l'aquifère rocheux régional en Montérégie Est, Québec. M.Sc. thesis, Université du Québec, Institut national de la recherche scientifique, Centre Eau Terre Environnement.

Benoît, N., D. Blanchette, M. Nastev, V. Cloutier, M. Parent, D. Marcotte, M. Brun Koné, and J.W.Molson. 2011. Groundwater Geochemistry of the Lower Chaudière River Watershed, Québec, Canada. In Proc. *Geohydro2011*, Joint IAH-CNC, CANQUA and AHQ conference, Quebec City, Canada, August 28-31, 2011, Paper DOC-2209, 8 p., 2011.

Benoît, N., J.W. Molson, M.Y. Brun Koné, and M. Nastev. 2015. *Modèle hydrogéologique 3D du bassin versant de la rivière Chaudière : Open File 7734*. Quebec: Geological Survey of Canada, 32 pp. doi:10.4095/295674.

Benoît, N., M. Nastev, D. Blanchette, and J. Molson. 2014. Hydrogeology and hydrogeochemistry of the Chaudière River watershed aquifers, Québec, Canada. *Canadian Water Resources Journal / Revue Canadienne Des Ressources Hydriques*, *39*(1): 32–48. https://doi.org/10.1080/07011784.2014.881589

Benoît, N., M. Nastev, D. Blanchette, and N. Roy. 2009. Hydrogéochimie du Bassin Versant de la Rivière Chaudière, Québec. In *Proceedings of the 62nd Annual Canadian Geological Society (CGS) and 10th Joint International Association of Hydrogeologists-Canadian National Chapter (IAH-CNC) Groundwater Specialty Conference*. Retrieved from http://www.researchgate.net/publication/258917782_Hydrogochimie_du_bassin_vers ant_de_la_rivire_Chaudire_Qubec/file/72e7e529657b66afaf.pdf

Bense, V.F., T. Gleeson, S.E. Loveless, O. Bour, and J. Scibek. 2013. Fault zone hydrogeology. *Earth-Science Reviews 127*: 171–192. https://doi.org/10.1016/j.earscirev.2013.09.008

Bethke, C.M., and T. M. Johnson. 2008. *Groundwater Age and Groundwater Age Dating (review-article)*. http://www.annualreviews.org.acces.bibl.ulaval.ca/doi/10.1146/annurev.earth.36.031 207.124210 (accessed April 7 2017).

Birdsell, D.T., H. Rajaram, D. Dempsey, and H.S.Viswanathan. 2015. Hydraulic fracturing fluid migration in the subsurface: A review and expanded modeling results. *Water Resources Research* 51(9): 7159–7188. https://doi.org/10.1002/2015WR017810

888 Bordeleau, G., C. Rivard, D. Lavoie, A. Mort, J. Ahad, X. Malet, and X. Xu. 2015.
889   Identifying the source of methane in groundwater in a 'virgin' area with regards to
890   shale gas exploitation: a multi-isotope approach. *Procedia Earth and Planetary*
891   *Science* 13: 219-222. doi:10.1016/j.proeps.2015.07.052.

892 Brun Koné, M. Y. 2013. Développement d'un modèle numérique d'écoulement 3D des
893   eaux souterraines du bassin versant de la Rivière Chaudière, Québec. M.Sc. thesis,
894   Université Laval. Retrieved from http://theses.ulaval.ca/archimede/meta/29257

895 Caine, J.S., J.P. Evans, and C.B. Forster. 1996. Fault zone architecture and permeability
896   structure. *Geology* 24(11): 1025–1028.

897 Caron, O. 2012. Synthèse et modèle cartographique 3D des Dépôts Quaternaires pour les
898   Bassins-Versants des Rivières Chaudière et Saint-François: Géochronologie,
899   Sédimentologie et Paléogéographie Wisconsinienne du sud du Québec. PhD diss.,
900   Université du Québec à Montréal.

901 Carrier, A., N. Benoît, M. Nastev, N. Roy, E. Beaudoin, P. Giguère, and P. Bouffard. 2014.
902   *Atlas des Eaux Souterraines du Bassin Versant de la Rivière Chaudière: Secteur de*
903   *la Basse-Chaudière et de la Moyenne-Chaudière: Dossier Public No. DP7284.*
904   Sainte-Marie: Commission Géologique du Canada, 199 pp.

905 Castonguay, S., J. Dietrich, D. Lavoie, and J.Y. Laliberté. 2010. Structure and petroleum
906   plays of the St. Lawrence Platform and Appalachians in southern Quebec: insights
907   from interpretation of MRNQ seismic reflection data. *Bulletin of Canadian*
908   *Petroleum Geology* 58(3): 219-234.

909 Canadian Council of Academies (CCA), Environmental Impacts of Shale Gas Extraction in
910   Canada, (J. Cherry, et al., Eds.), May 2014,
911   http://www.scienceadvice.ca/en/assessments/completed/shale-gas.aspx.

912 Cloutier, V., R. Lefebvre, M.M. Savard, and R. Therrien. 2010. Desalination of a
913   sedimentary rock aquifer system invaded by Pleistocene Champlain Sea water and
914   processes controlling groundwater geochemistry. *Environmental Earth Sciences*
915   59(5): 977–994. https://doi.org/10.1007/s12665-009-0091-8

916 Cloutier, V., R. Lefebvre, M.M. Savard, É. Bourque, and R. Therrien. 2006.
917   Hydrogeochemistry and groundwater origin of the Basses-Laurentides sedimentary
918   rock aquifer system, St. Lawrence Lowlands, Québec, Canada. *Hydrogeology*
919   *Journal* 14(4): 573–590. https://doi.org/10.1007/s10040-005-0002-3

920 Cloutier, V., R. Lefebvre, R. Therrien, and M. M. Savard. 2008. Multivariate statistical
921   analysis of geochemical data as indicative of the hydrogeochemical evolution of
922   groundwater in a sedimentary rock aquifer system. *Journal of Hydrology* 353(3–4):
923   294–313. https://doi.org/10.1016/j.jhydrol.2008.02.015

924   Cochand, F. 2014. Impact des changements climatiques et du développement urbain sur les
925   ressources en eaux du bassin versant de la rivière Saint-Charles. PhD diss., Université
926   Laval.

927   Goderniaux, P., Davy, P., Bresciani, E., de Dreuzy, J.-R., Le Borgne, T., 2013. Partitioning
928   a regional groundwater flow system into shallow local and deep regional flow
929   compartments. Water Resour. Res. 49, 2274–2286.
930
931   Croteau, A., M. Nastev, and R. Lefebvre. 2010. Groundwater recharge assessment in the
932   Chateauguay River watershed. *Canadian Water Resources Journal* 35(4): 451-468.

933   Crow, H. L., and P. Ladevèze. 2015. *Downhole geophysical data collected in 11 boreholes
934   near St-Édouard-de-Lotbinière: Open file 7768*. Québec: Geological Survey of
935   Canada, 48 pp.

936   Doherty, J. 2015. *Calibration and Uncertainty Analysis for Complex Environmental
937   Models*. Brisbane, Australia: Watermark Numerical Computing.

938   Domenico, P. A., and F. W. Schwartz. 1998. *Physical and Chemical Hydrogeology* (Vol.
939   506). New York: Wiley.

940   Flewelling, S. A., and M. Sharma. 2014. Constraints on upward migration of hydraulic
941   fracturing   fluid   and   brine.   *Groundwater*   52(1):   9–19.
942   https://doi.org/10.1111/gwat.12095

943   Freeze, R. A., and J. A. Cherry. 1979. *Groundwater*, 604 pp.

944   Gassiat, C., T. Gleeson, R. Lefebvre, and J. McKenzie. 2013. Hydraulic fracturing in
945   faulted sedimentary basins: Numerical simulation of potential contamination of
946   shallow aquifers over long time scales. *Water Resources Research* 49(12): 8310–
947   8327. https://doi.org/10.1002/2013WR014287

948   Globensky, Y. 1987. *Geology of the St. Lawrence Lowlands MM, 85-02*. Quebec: Quebec
949   Ministry of Energy and Resources.

950   Goode, D. J. 1996. Direct Simulation of Groundwater Age. *Water Resources Research*
951   32(2): 289–296. https://doi.org/10.1029/95WR03401

952   Graf, T. 2015. Physically-based assessment of intrinsic groundwater resource vulnerability.
953   PhD diss., Université Laval.

954   Grasby, S.E., D.M. Allen, S. Bell, Z. Chen, G. Ferguson, A. Jessop, M. Kelman, M. Ko, J.
955   Majorowicz, M. Moore, J. Raymond, R. Therrien. 2011. *Geothermal Energy
956   Resource Potential of Canada: Open File 6914*. Ottawa: Geological Survey of
957   Canada.

958   Hayley, K., J. Schumacher, G.J. MacMillan, and L.C. Boutin. 2014. Highly parameterized
959   model calibration with cloud computing: an example of regional flow model
960   calibration in northeast Alberta, Canada. *Hydrogeology Journal* 22(3): 729–737.
961   https://doi.org/10.1007/s10040-014-1110-8

962   Hiscock, K.M., and V.F. Bense. 2014. *Hydrogeology: Principles and Practice*. Chichester:
963   John Wiley and Sons.

964   Institut de la Statistique Québec (ISQ). 2017. *Population du Québec, 1971-2016.*
965   http://www.stat.gouv.qc.ca/statistiques/population-demographie/structure/qc_1971-
966   20xx.htm (accessed May, 2017).

967   Janos, D., 2017. Regional Groundwater Flow Dynamics and Residence Times in
968   Chaudière-Appalaches, Québec, Canada: Insights from Numerical Simulations, MSc.
969   Thesis. Université Laval.

970   Kazemi, G.A., J. H. Lehr, and P. Perrochet. 2006. *Groundwater Age*. Hoboken: John Wiley
971   and Sons, 325 pp.

972   Kissinger, A., R. Helmig, A. Ebigbo, H. Class, T. Lange, M. Sauter, M. Heitfeld, J.
973   Klünker, and W. Jahnke. 2013. Hydraulic fracturing in unconventional gas reservoirs:
974   risks in the geological system, part 2. *Environmental Earth Sciences* 70(8): 3855–
975   3873. https://doi.org/10.1007/s12665-013-2578-6

976   Ladevèze, P. 2017. Aquifères de surface et ressources profondes: le rôle des failles et des
977   réseaux de fractures naturelles sur la circulation de fluides. Ph.D. diss., Université du
978   Québec, Institut national de la recherche scientifique, Centre Eau Terre
979   Environnement.

980   Ladevèze, P., C. Rivard, R. Lefebvre, D. Lavoie, M. Parent, X. Malet, G. Bordeleau, and
981   J.S. Gosselin. 2016. *Travaux de caractérisation hydrogéologique dans la plateforme
982   sédimentaire du Saint-Laurent, région de Saint-Édouard-de-Lotbinière, Québec:
983   Dossier public 8036.* Québec: Commission géologique du Canada, 112 pp.
984   doi:10.4095/297891

985   Ladevèze, P., S. Séjourné, C. Rivard, R. Lefebvre, and D. Lavoie. 2017. Faults and natural
986   fractures potential control on upward fluid migration: insights from a shale gas play
987   in the St. Lawrence Platform, Canada. Submitted to *Hydrogeology Journal* in July
988   2017.

989   Lange, T., M. Sauter, M. Heitfeld, K. Schetelig, K. Brosig, W. Jahnke, A. Kissinger, R.
990   Helmig, A. Ebigbo, and H. Class. 2013. Hydraulic fracturing in unconventional gas
991   reservoirs: risks in the geological system part 1. *Environmental Earth Sciences* 70(8):
992   3839–3853. https://doi.org/10.1007/s12665-013-2803-3

993   Laurencelle, M., R. Lefebvre, C. Rivard, M. Parent, P. Ladevèze, N. Benoît, M.-A. Carrier.
994   2013. Modeling the evolution of the regional fractured-rock aquifer system in the

36

995   Northern Lake Champlain watershed following last deglaciation. *GéoMontréal2013*,
996   *66th Canadian Geotechnical Conference* and the *11th Joint CGS/IAH-CNC
997   Groundwater Conference*, Montreal, Quebec, Canada, Sept. 29 to Oct. 3, 2013.

998   Lavigne, M.-A., M. Nastev, R. Lefebvre. 2010. Numerical simulation of groundwater flow
999   in the Chateauguay River aquifers. *Canadian Water Resources Journal* 35(4): 469-
1000   486.

1001   Lavoie, D., N. Pinet, G. Bordeleau, O.H. Ardakani, P. Ladevèze, M.J. Duchesne, C. Rivard,
1002   A. Mort, V. Brake, H. Sanei, and X. Malet. 2016. The Upper Ordovician black shales
1003   of southern Quebec (Canada) and their significance for naturally occurring
1004   hydrocarbons in shallow groundwater. *International Journal of Coal Geology* 158:
1005   44–64. https://doi.org/10.1016/j.coal.2016.02.008

1006   Lavoie, D., C. Rivard, R. Lefebvre, S. Séjourné, R. Thériault, M.J. Duchesne, J. Ahad, B.
1007   Wang, N. Benoît, and C. Lamontagne. 2014) The Utica Shale and gas play in
1008   southern Quebec: Geological and hydrogeological synthesis and methodological
1009   approaches to groundwater risk evaluation. *International Journal of Coal Geology
1010   (IJCG)* 126: 77-91, Special issue on potential environmental impacts of
1011   unconventional fossil energy development, D.J. Soeder and M.A. Engle, Ed., doi:
1012   10.1016/j.coal.2013.10.011.

1013   Lefebvre, R. 2017. Mechanisms leading to potential impacts of shale gas development on
1014   groundwater quality. *Wiley Interdisciplinary Reviews: Water* 4(1): January/February
1015   2017, 15 p. doi: 10.1002/wat2.1188.

1016   Lefebvre, R., J.M. Ballard, M.-A. Carrier, H. Vigneault, C. Beaudry, L. Berthot, G. Légaré-
1017   Couture, M. Parent, M. Laurencelle, X. Malet, and A. Therrien. 2015. *Portrait des
1018   ressources en eau souterraine en Chaudière-Appalaches, Québec, Canada (No.
1019   Rapport final INRS R-1508)*. Projet réalisé conjointement par l'Institut national de la
1020   recherche scientifique (INRS), l'Institut de recherche et développement en
1021   agroenvironnement (IRDA) et le Regroupement des organismes de bassins versants
1022   de la Chaudière-Appalaches (OBV-CA) dans le cadre du Programme d'acquisition de
1023   connaissances sur les eaux souterraines (PACES).

1024   McCormack, R. 1982. *Étude hydrogéologique du bassin de la Chaudière* (Programme de
1025   connaissance intégrées No. EI-1). Québec: Ministère de l'Environnement du Québec,
1026   Direction générale des inventaires et de la recherche.

1027   Ministère du Développement durable, de l'Environnement et de la Lutte contre les
1028   changements climatiques, MDDELCC. 2017. Programme d'acquisition de
1029   connaissances sur les eaux souterraines.
1030   http://www.mddelcc.gouv.qc.ca/eau/souterraines/programmes/acquisition-
1031   connaissance.htm (accessed May, 2017).

1032   Molson, J.W. and E.O. Frind. 2017. *FLONET/TR2 User Guide, A Two-Dimensional
1033   Simulator for Groundwater Flownets, Contaminant Transport and Residence Time,
1034   Version 5*. Université Laval and University of Waterloo, 57 pp.

37

Molson, J.W., and E.O. Frind. 2012. On the use of mean groundwater age, life expectancy and capture probability for defining aquifer vulnerability and time-of-travel zones for source water protection. *Journal of Contaminant Hydrology* 127(1): 76-87. doi:10.1016/j.jconhyd.2011.06.001.

Montcoudiol, N., J. Molson, and J.-M. Lemieux, Numerical modelling in support of a conceptual model for groundwater flow and geochemical evolution in the southern Outaouais Region, Quebec, Canada. *Canadian Water Resources Jour.*, Special Issue on Quebec PACES Projects, http://www.tandfonline.com/doi/full/10.1080/07011784.2017.1323560, 2017.

Montcoudiol, N., J. Molson, J.-M. Lemieux, and V. Cloutier. 2015. A conceptual model for groundwater flow and geochemical evolution in the southern Outaouais Region, Québec, Canada. *Applied Geochemistry* 58: 62–77. https://doi.org/10.1016/j.apgeochem.2015.03.007

Moritz, A., J.F. Hélie, D.L. Pinti, M. Larocque, D. Barnetche, S. Retailleau, R. Lefebvre, and Y. Gélinas. 2015. Methane Baseline Concentrations and Sources in Shallow Aquifers from the Shale Gas-Prone Region of the St. Lawrence Lowlands (Quebec, Canada). *Environmental Science and Technology* 49(7): 4765–4771. https://doi.org/10.1021/acs.est.5b00443

Nastev, M., A. Rivera, R. Lefebvre, R. Martel, and M. Savard. 2005. Numerical simulation of groundwater flow in regional rock aquifers, southwestern Quebec, Canada. *Hydrogeology Journal* 13(5): 835-848.

Nastev, M., M.M. Savard, P. Lapcevic, R. Lefebvre, and R. Martel. 2004. Hydraulic properties and scale effects investigation in regional rock aquifers, south-western Quebec, Canada. *Hydrogeology Journal* 12(3): 257–269. https://doi.org/10.1007/s10040-004-0340-6

Ngoc, T.D.T., R. Lefebvre, E. Konstantinovskaya, and M. Malo. 2014. Characterization of deep saline aquifers in the Bécancour area, St. Lawrence Lowlands, Québec, Canada: implications for CO_2 geological storage. *Environmental Earth Sciences* 1–28. https://doi.org/10.1007/s12665-013-2941-7

Nowamooz, A., J.-M. Lemieux, J. Molson, and R. Therrien. 2015. Numerical investigation of methane and formation fluid leakage along the casing of a decommissioned shale gas well. *Water Resources Research* 51(6): 4592–4622. https://doi.org/10.1002/2014WR016146

Parent, M., and S. Occhietti. 1988. Late Wisconsinan deglaciation and Champlain Sea invasion in the St. Lawrence Valley, Québec. *Géographie Physique et Quaternaire* 42(3): 215–246. https://doi.org/10.7202/032734ar

Pinti, D.L., Y. Gélinas, M. Larocque, D. Barnetche, S. Retailleau, A. Moritz, J. Hélie, and R. Lefebvre. 2013. *Concentrations, sources et mécanismes de migration*

1073   *préférentielle des gaz d'origine naturelle (méthane, hélium, radon) dans les eaux*
1074   *souterraines des Basses-Terres du Saint-Laurent. Volet Géochimie. Étude E3-9,*
1075   *FQRNT ISI n° 171083*. UQAM, U. Concordia, INRS-ETE, 94 pp.

1076   Révész, K.M., K.J. Breen, A.J. Baldassare, and R.C. Burruss. 2010. Carbon and hydrogen
1077   isotopic evidence for the origin of combustible gases in water-supply wells in north-
1078   central   Pennsylvania.   *Applied   Geochemistry*   25(12):   1845–1859.
1079   https://doi.org/10.1016/j.apgeochem.2010.09.011

1080   Rivard, C., D. Lavoie, R. Lefebvre, S. Séjourné, C. Lamontagne, E.G. Johnson, M.J.
1081   Duchesne. 2014. An overview of Canadian shale gas production and environmental
1082   concerns. Online December 18, 2013, *International Journal of Coal Geology (IJCG)*
1083   126 (2014): 64-76. doi: 10.1016/j.coal.2013.12.004.

1084   Rousseau, A.N., A. Mailhot, M. Slivitzky, J.-P. Villeneuve, M.J. Rodriguez, and A.
1085   Bourque. 2004. Usages et approvisionnement en eau dans le sud du Québec Niveau
1086   des connaissances et axes de recherche à privilégier dans une perspective de
1087   changements climatiques. *Canadian Water Resources Journal / Revue Canadienne*
1088   *Des Ressources Hydriques* 29(2): 121–134. https://doi.org/10.4296/cwrj121

1089   Roy, N., J. Molson, J.-M. Lemieux, D. Van Stempvoort, and A. Nowamooz. 2016. Three-
1090   dimensional numerical simulations of methane gas migration from decommissioned
1091   hydrocarbon production wells into shallow aquifers. *Water Resources Research*
1092   52(7): 5598–5618. https://doi.org/10.1002/2016WR018686

1093   Saby, M., M. Larocque, D.L. Pinti, F. Barbecot, Y. Sano, and M.C. Castro. 2016. Linking
1094   groundwater quality to residence times and regional geology in the St. Lawrence
1095   Lowlands, southern Quebec, Canada. *Applied Geochemistry* 65: 1–13.
1096   https://doi.org/10.1016/j.apgeochem.2015.10.011

1097   Schulze-Makuch, D. 2005. Longitudinal dispersivity data and implications for scaling
1098   behavior. *Ground Water* 43(3): 443–456. https://doi.org/10.1111/j.1745-
1099   6584.2005.0051.x

1100   Schulze-Makuch, D., D.A. Carlson, D.S. Cherkauer, and P. Malik. 1999. Scale dependency
1101   of hydraulic conductivity in heterogeneous media. *Ground Water* 37(6): 904–919.
1102   https://doi.org/10.1111/j.1745-6584.1999.tb01190.x

1103   Scibek, J., T. Gleeson, and J.M. McKenzie. 2016. The biases and trends in fault zone
1104   hydrogeology conceptual models: global compilation and categorical data analysis.
1105   *Geofluids* 16(4): 782–798. https://doi.org/10.1111/gfl.12188

1106   Séjourné, S., R. Lefebvre, X. Malet, and D. Lavoie. 2013. *Synthèse géologique et*
1107   *hydrogéologique du Shale d'Utica et des unités sus-jacentes (Lorraine, Queenston et*
1108   *dépôts meubles), Basses-Terres du Saint-Laurent, Québec (No. 7338)*. Québec:
1109   Commission   géologique   du   Canada.   Retrieved   from
1110   http://geoscan.ess.nrcan.gc.ca/cgi-

39

1111   bin/starfinder/0?path=geoscan.flandid=fastlinkandpass=andsearch=R%3D292430and
1112   format=FLFULL

1113 Siade, A., T. Nishikawa, and P. Martin. 2015. Natural recharge estimation and uncertainty
1114   analysis of an adjudicated groundwater basin using a regional-scale flow and
1115   subsidence model (Antelope Valley, California, USA). *Hydrogeology Journal* 23(6):
1116   1267–1291. https://doi.org/10.1007/s10040-015-1281-y

1117 Slivitzky, A., and P. St-Julien. 1987. *Compilation géologique de la région de l'Estrie-*
1118   *Beauce*. Québec: Ministère de l'énergie et des ressources, Direction générale de
1119   l'exploration géologique et minérale, Direction de la recherche géologique, Service
1120   de la géologie.

1121 Tecsult. 2008. *Cartographie hydrogéologique du bassin versant de la rivière Chaudière -*
1122   *Secteurs de la Basse-Chaudière et de la Moyenne-Chaudière*. Étude réalisée dans le
1123   cadre du Projet eaux souterraines de la Chaudière, financé par le Programme
1124   d'approvisionnement en eau Canada, Québec (PAECQ) et géré par le Conseil pour
1125   le développement de l'agriculture du Québec (CDAQ), 142 pp.

1126 Thériault, R. 2012. *Caractérisation du Shale d'Utica et du Groupe de Lorraine, Basses-*
1127   *Terres du Saint-Laurent-Partie 1: Compilation des données DV 2012-3*. Québec:
1128   Ministère des Ressources naturelles et de la Faune, SIGEOM, 212 pp.

1129 Tóth, J. 1999. Groundwater as a geologic agent: An overview of the causes, processes, and
1130   manifestations.   *Hydrogeology*   *Journal*   7(1):   1–14.
1131   https://doi.org/10.1007/s100400050176

1132 Tóth, J. 2009. *Gravitational systems of groundwater flow: theory, evaluation, utilization*.
1133   Cambridge University Press. doi:10.1017/CBO9780511576546.

1134 Vautour, G., D.L. Pinti, P. Méjean, M. Saby, G. Meyzonnat, M. Larocque, M.C. Castro,
1135   C.M. Hall, C. Boucher, E. Roulleau, and F. Barbecot, N. Takahata, Y. Sano. 2015.
1136   3H/3He, 14C and (U–Th)/He groundwater ages in the St. Lawrence Lowlands,
1137   Quebec,   Eastern   Canada.   *Chemical*   *Geology*   *413*:   94–106.
1138   https://doi.org/10.1016/j.chemgeo.2015.08.003

1139 Vengosh, A., R.B. Jackson, N. Warner, T.H. Darrah, and A. Kondash. 2014. A critical
1140   review of the risks to water resources from unconventional shale gas development
1141   and hydraulic fracturing in the United States. *Environmental Science and Technology*
1142   48(15): 8334–8348. https://doi.org/10.1021/es405118y.

1143 Vogel, 1967. Investigation of groundwater flow with radiocarbon, *Isotopes in Hydrology*,
1144   International Atomic Energy Agency, p355-368.
1145 Warner, N.R., R.B. Jackson, T.H Darrah, S.G. Osborn, A. Down, K. Zhao, A. White, and
1146   A. Vengosh. 2012. Geochemical evidence for possible natural migration of Marcellus

1147 Formation brine to shallow aquifers in Pennsylvania. *Proceedings of the National*
1148   *Academy of Sciences* 109(30): 11961–11966.

1149 Xu, M., and Y. Eckstein. 1995. Use of weighted least-squares method in evaluation of the
1150   relationship between dispersivity and field scale. *Ground Water* 33(6): 905–908.
1151   https://doi.org/10.1111/j.1745-6584.1995.tb00035.x

1152 Zhang, Y., C.W. Gable, and M. Person. 2006. Equivalent hydraulic conductivity of an
1153   experimental stratigraphy: Implications for basin-scale flow simulations. *Water*
1154   *Resources Research* 42(5): W05404. https://doi.org/10.1029/2005WR004720

1155 Zhu, J., C.L. Winter, and Z. Wang. 2015. Nonlinear effects of locally heterogeneous
1156   hydraulic conductivity fields on regional stream–aquifer exchanges. *Hydrology ans*
1157   *Earth System Sciences* 19(11): 4531–4545. https://doi.org/10.5194/hess-19-4531-
1158   2015

1159 Zijl, W. 1999. Scale aspects of groundwater flow and transport systems. *Hydrogeology*
1160   *Journal* 7(1): 139–150. https://doi.org/10.1007/s100400050185

1161

41

List of Figures

Figure 1. Location and topography of the Chaudière-Appalaches study area, and location of the 2D regional cross-section model, modified from Lefebvre et al. (2015)

Figure 2. Conceptual model for the Chaudière-Appalaches regional groundwater model, showing a) flow and geochemical evolution with water types G1, G2 and G3, and b) the geologic cross-section of the deep subsurface (after Séjourné et al. 2013).

Figure 3. Vertical distribution of measured and model-generated hydraulic conductivities in the Chaudière-Appalaches region. Grey dots represent estimated values from the well drillers' log (Lefebvre et al. 2015). Black squares show the median measured value per 5 meter intervals and the horizontal whiskers show the 25th and 75th percentiles. Solid lines show the calibrated distribution of hydraulic conductivities in the fractured bedrock and dashed lines show different conductivity scenarios tested in the sensitivity analysis of Janos (2017).

Figure 4. Geological structure, hydraulic conductivities and boundary conditions for the numerical flow model.

Figure 5. Model calibration: Observed heads (from interpolated regional piezometry) against simulated heads.

Figure 6. Calibrated recharge fluxes, simulated hydraulic heads, observed water table elevations (from interpolated piezometry) and topographic elevation along the model cross-section. Negative fluxes are exiting the model domain and positive fluxes are entering (corresponding to recharge).

Figure 7. Calibrated steady-state flow model showing hydraulic heads and streamline distribution

Figure 8. Calibrated flow model a) Zoom 1 (Appalachian Highlands), b) Zoom 2 (St. Lawrence Lowlands close to St. Lawrence River), c) Zoom 3 (St. Lawrence Lowlands close to Appalachian front), showing hydraulic heads and streamline distribution (location shown in Fig. 7).

Figure 9. Simulated steady-state mean groundwater ages with superimposed streamlines from the calibrated flow model. (Plot enlargements for Zooms 1, 2 and 4 are provided in Figure 10; Zooms 3 and 5 can be found in Janos, 2013).

Figure 10 Simulated mean groundwater ages with superimposed streamlines from the calibrated flow model a) Zoom 1, b) Zoom 2, c) Zoom 4. (Locations shown in Fig. 9).

Figure 11 Conceptual model of the Jacques-Cartier River fault zone. Vertical hydraulic conductivities shown correspond to scenario P of the parametric study on faults.

Figure12. Steady-state flow model showing hydraulic conductivities in the horizontal direction and streamlines for fault scenarios described in Table 4, vertical exaggeration is 1.25×.

42

1199   Figure 13. Steady-state flow and age transport model showing mean groundwater and
1200   streamlines for fault scenarios described in Table 4, vertical exaggeration is 1.25×.

1201

1202 Table 1. Physical description of the surficial deposits, including reported and calibrated
1203 hydraulic conductivities.

Mod. Unit	Geologic Group /Description	Hydraulic Description	Reported Log K (m/s)			Reference	Calibrated log K (m/s)
org	Organic deposits (phagnum and ericaceous peat)	Poorly drained		-4.52		Tecsult (2008)	-4.73
				-5.00		Brun Koné (2013)	
				-6.48		Ladevèze (2015)	
all	Alluvium (silt and sand)	permeable		-4.00		Tecsult (2008)	-6.00
			-6.00	to	-3.00	Brun Koné (2013)	
			-7.44	to	-4.06	Ladevèze (2015)	
			-9.00	to	-4.70	Domenico and Schwartz (1998)	
lgd	Lakeshore delta (sand, silts, gravel)	permeable	-6.00	to	-3.00	Brun Koné (2013)	-6.00
			-6.70	to	-3.52	Domenico and Schwartz (1998)	
mgd	Glaciomarine delta (sand, silts, gravel)	permeable	-6.00	to	-3.00	Brun Koné (2013)	-5.9
			-6.70	to	-3.52	Domenico and Schwartz (1998)	
mgbg	Littoral glaciomarine (coarse) (gravel, sand, silts)	permeable		-4.00		Tecsult (2008)	-4.4
			-6.00	to	-3.00	Brun Koné (2013)	
			-8.12	to	-5.27	Ladevèze (2015)	
			-6.70	to	-3.52	Domenico and Schwartz (1998)	
mgbf	Littoral glaciomarine (fine) (silts, sand, gravel)	relatively permeable		-4.00		Tecsult (2008)	-5.97
			-6.00	to	-3.00	Brun Koné (2013)	
			-8.12	to	-5.27	Ladevèze (2015)	
			-6.70	to	-3.52	Domenico and Schwartz (1998)	
grav	Glaical/fluvioglacial (sand and gravel)	very permeable		-3.52		Tecsult (2008)	-3.96
			-6.00	to	-3.00	Brun Koné (2013)	
			-6.70	to	-3.52	Domenico and Schwartz (1998)	
till	Glacial tills (sand, silt, clay)	spatially variable		-8.52		Tecsult (2008)	-6.05
				-8.70		Tecsult (2008)	
				-6.22		Brun Koné (2013)	
			-12.00	to	-5.70	Domenico and Schwartz (1998)	
sab	Sand	permeable		-6.52		Tecsult (2008)	-4.86
				-7.00		Brun Koné (2013)	
			-9.00	to	-5.00	Ladevèze (2015)	
			-8.10	to	-3.52	Domenico and Schwartz (1998)	

1204

1205

44

Table 2. Description of the modeled geologic rock units, including the reported and modeled hydraulic conductivities and porosities (includes properties reported by Gassiat et al. 2013). Bedrock anisotropy obtained from Freeze & Cherry (1979).

Model Unit	Geologic Group	Literature Description	log K (m/s) min to max	Por. (%)	Reference
Above Shale in SLP	Lorraine *silty shales with mostly non calcareous sediments interbedded with fine sandstone and clayey siltstones*	Fine grained sedimentary[a]	-10.21 to -6.71		Gleeson et al. (2011)
		Lorraine unit matrix Bécancour (eastern Canada)[a,b]	-10.61	3.9	Tran Ngoc et al. (2014)
		Fractured rock[c]	-6.47 to -4.96		Ladevèze (2015) Personal communication
		Fractured rock in St. Lawrence Platform formation	-9.43 to -3.19		Lefebvre et al. (2015)
		Minimum values in model (log Kx/log Kz)	**-9.01/-10.01**	**5**	
Above Shale in AH	Humber zone *carbonates, sandstones and shales*	Fractured rock	-8.96 to -5.39		Ladevèze (2015) Personal communication
		Fractured rock in Humber formation	-11.28 to -2.03		Lefebvre et al. (2015)
		Minimum values in model (log Kx/log Kz)	**-8.98/-9.68**	**5**	
Utica Shale	Utica shale *calcareous black shale*	General[a]	-15.21 to -9.21		Neuzil (1994)
		General[a]	-12.21 to -8.21		Freeze and Cherry (1979)
		General[a]	-15.21 to -12.21		Flewelling and Sharma (2013)
		Utica (eastern Canada)[a]	-14.26 to -8.31		Séjouné et al. (2005)
		Marcellus (Northeastern USA)	-7.91		Soeder (1988)
		Barnett	-9.21		Montgomery et al.(2005)
		Utica unit Bécancour matrix (eastern Canada)[a,b]	-10.73	4	Tran Ngoc et al. (2014)
		log Kx/log Kz in model	**-9.5/-11.5**	**5**	
Carbonate Platform	Trenton *clayey limestone interbedded with shales*	Trenton unit Bécancour matrix (eastern Canada)[a,b]	-7.81	3.4	Tran Ngoc et al. (2014)
		Trenton unit Bécancour global (eastern Canada)[a,b]	-5.10		Tran Ngoc et al. (2014)
	Black River	*limestone interbedded with sandstone*			
	Chazy	*clayey and sandy limestone*			
	Beakmantown *dolomitic sandstone becoming pure dolostone then dolomitic limestone*	Beauharnois unit Bécancour matrix (eastern Canada)[a,b]	-8.26	1	Tran Ngoc et al. (2014)
		Beauharnois unit Bécancour global (eastern Canada)[a,b]	-8.43		Tran Ngoc et al. (2014)
		Theresa unit Bécancour matrix (eastern Canada)[a,b]	-8.43	2.6	Tran Ngoc et al. (2014)
		Theresa unit Bécancour global (eastern Canada)[a,b]	-8.10		Tran Ngoc et al. (2014)
	Potsdam *poorly cemented sandstone formation becoming well cemented*	Cairnside unit Bécancour matrix (eastern Canada)[a,b]	-8.13	3.3	Tran Ngoc et al. (2014)
		Cairnside unit Bécancour global (eastern Canada)[a,b]	-6.59		Tran Ngoc et al. (2014)
		Covey Hill unit Bécancour matrix (eastern Canada)[a,b]	-7.83	6.3	Tran Ngoc et al. (2014)
		Values in model	**-8/-9**	**1**	
Grenville	Grenville *unfractured metamorphic and igneous*	Crystalline[a]	-9.21 to -4.71		Gleeson et al. (2011)
		Unfractured metamorphic and igneous rock	-12.21 to -8.71		Freeze and Cherry (1979)
		Calibrated hydraulic conductivities in Outaouais	-12 to -6.	1-3	Montcoudiol et al. (2017)
		log Kx/log Kz in model	**-11/-11**	**0.05**	

a- Calculated from permeability values using density = 1000 kg/m^3, viscosity = 8.90×10^{-4} Pa·s and g = 9.81 m/s^2, b- Median value given in study

Table 3. Average recharge to the bedrock calibrated from the HELP model and from the current 2-D flow model (SLL = St. Lawrence Lowlands, AHL=Appalachian Highlands).

Average recharge to the bedrock	Modeled with HELP (Lefebvre et al. 2015)	Calibrated flow model	% Absolute Error
Overall (mm/year)	166	164	1.04
SLL (mm/year)	85 (<15 to >300)	63	25.64
AHL (mm/year)	187 (100 to >300)	326	74.27

46

Table 4. Simulated fault permeability scenarios

Scenario	Fault Core (FC) hydraulic conductivity contrast with protolith (P) in x and z directions	Damage Zone (DZ) hydraulic conductivity contrast with protolith (P) in x and z directions	Fault Zone Permeability Conceptual Model
A	$K_{FC} = K_P$	$K_{DZ} = K_P$	Base Case
B	$K_{FC} = K_P$ x 0.1	$K_{DZ} = K_P$	Barrier
C	$K_{FC} = K_P$ x 0.01	$K_{DZ} = K_P$	Barrier
D	$K_{FC} = K_P$ x 0.001	$K_{DZ} = K_P$	Barrier
E	$K_{FC} = K_P$	$K_{DZ} = K_P$ x 10	Conduit
F	$K_{FC} = K_P$ x 0.1	$K_{DZ} = K_P$ x 10	Conduit-Barrier-Conduit
G	$K_{FC} = K_P$ x 0.01	$K_{DZ} = K_P$ x 10	Conduit-Barrier-Conduit
H	$K_{FC} = K_P$ x 0.001	$K_{DZ} = K_P$ x 10	Conduit-Barrier-Conduit
I	$K_{FC} = K_P$	$K_{DZ} = K_P$ x 100	Conduit
J	$K_{FC} = K_P$ x 0.1	$K_{DZ} = K_P$ x 100	Conduit-Barrier-Conduit
K	$K_{FC} = K_P$ x 0.01	$K_{DZ} = K_P$ x 100	Conduit-Barrier-Conduit
L	$K_{FC} = K_P$ x 0.001	$K_{DZ} = K_P$ x 100	Conduit-Barrier-Conduit
M	$K_{FC} = K_P$	$K_{DZ} = K_P$ x 1000	Conduit
N	$K_{FC} = K_P$ x 0.1	$K_{DZ} = K_P$ x 1000	Conduit-Barrier-Conduit
O	$K_{FC} = K_P$ x 0.01	$K_{DZ} = K_P$ x 1000	Conduit-Barrier-Conduit
P	$K_{FC} = K_P$ x 0.001	$K_{DZ} = K_P$ x 1000	Conduit-Barrier-Conduit
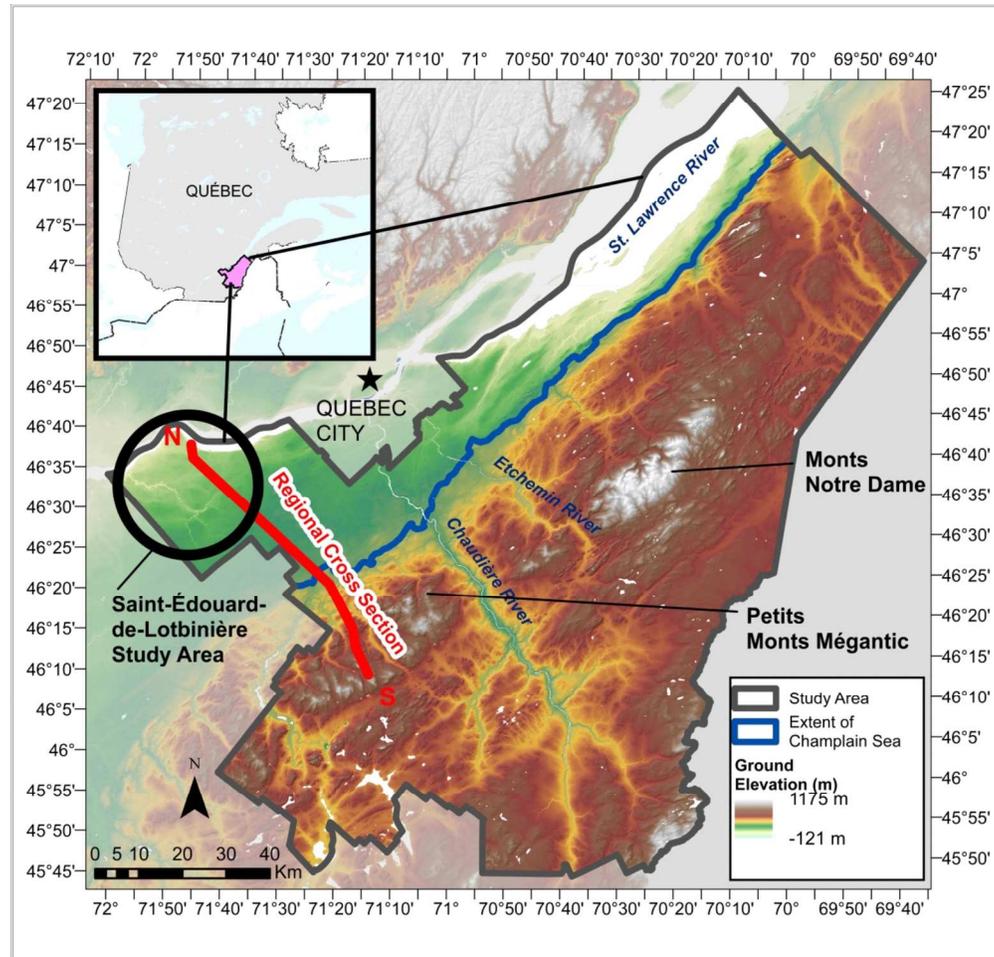
Figure 1. Location and topography of the Chaudière-Appalaches study area, and location of the 2D regional cross-section model, modified from Lefebvre et al. (2015)

152x165mm (300 x 300 DPI)
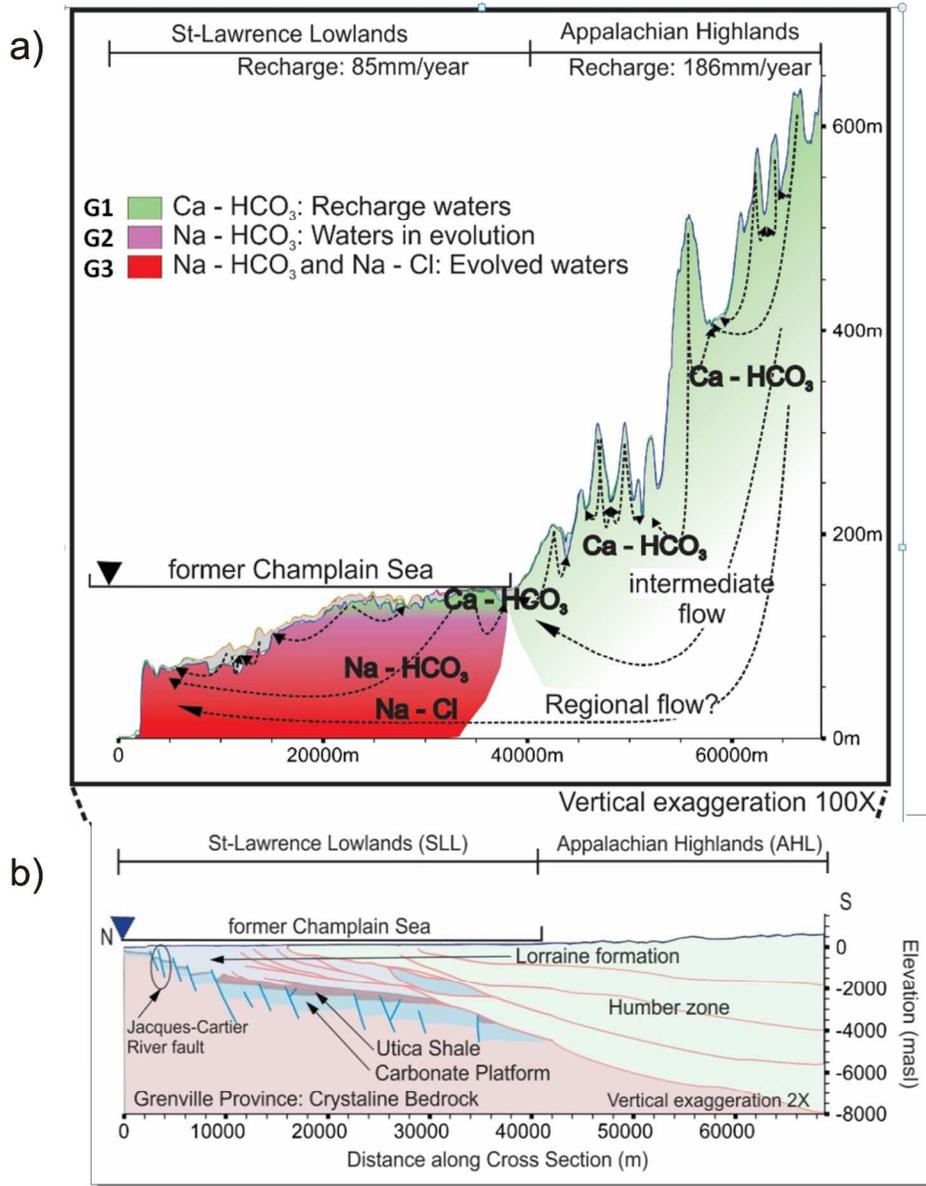
Figure 2. Conceptual model for the Chaudière-Appalaches regional groundwater model, showing a) flow and geochemical evolution with water types G1, G2 and G3, and b) the geologic cross-section of the deep subsurface (after Séjourné et al. 2013).

152x194mm (300 x 300 DPI)
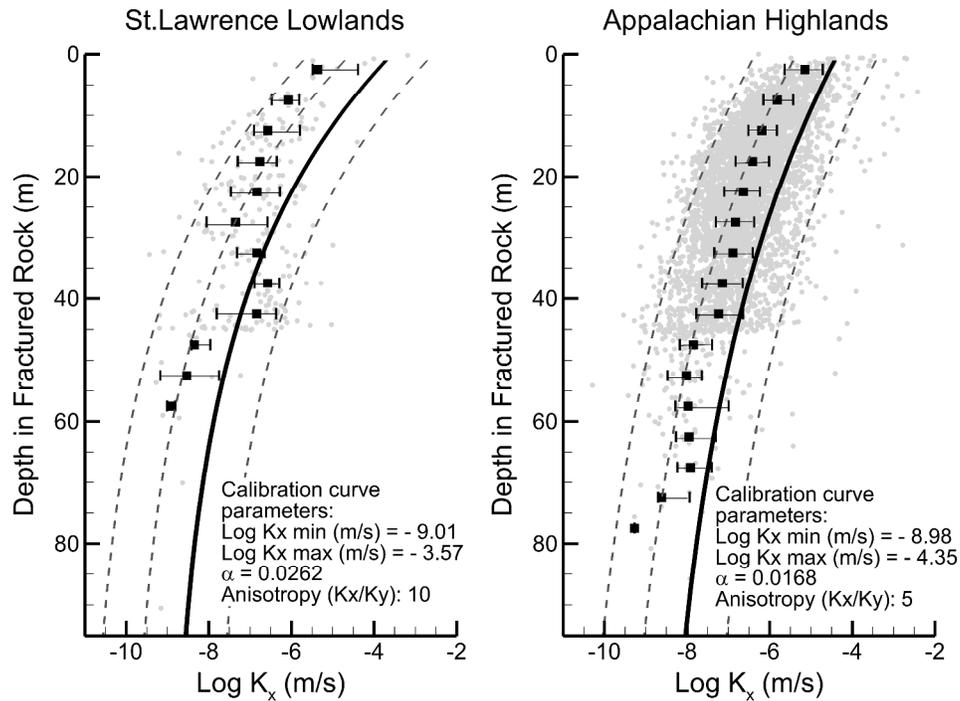
Figure 3. Vertical distribution of measured and model-generated hydraulic conductivities in the Chaudière-Appalaches region. Grey dots represent estimated values from the well drillers' log (Lefebvre et al. 2015). Black squares show the median measured value per 5 meter intervals and the horizontal whiskers show the 25th and 75th percentiles. Solid lines show the calibrated distribution of hydraulic conductivities in the fractured bedrock and dashed lines show different conductivity scenarios tested in the sensitivity analysis of Janos (2017).

1322x1006mm (96 x 96 DPI)
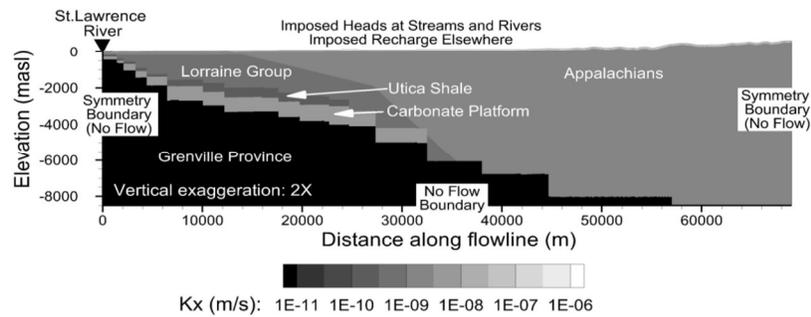
Figure 4. Geological structure, hydraulic conductivities and boundary conditions for the numerical flow model.

Figure 4. Geological structure, hydraulic conductivities and boundary conditions for the numerical flow model.

543x278mm (300 x 300 DPI)
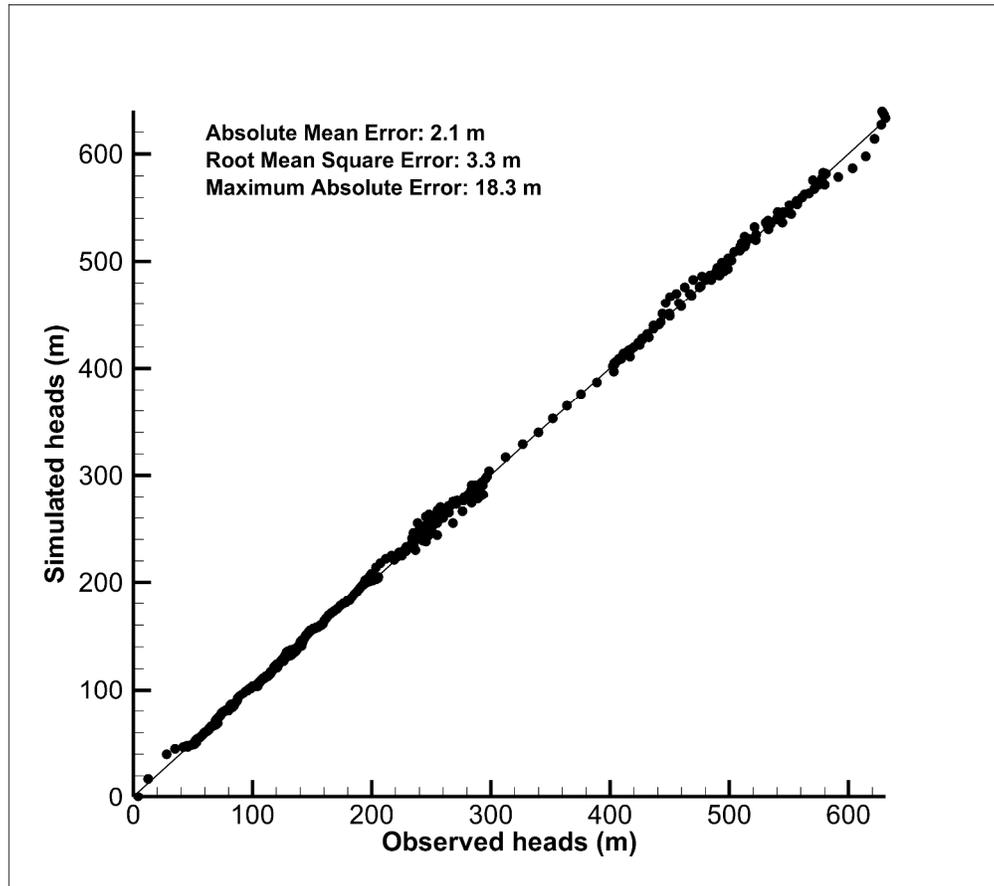
Figure 5. Model calibration: Observed heads (from interpolated regional piezometry) against simulated heads.

1322x1176mm (96 x 96 DPI)
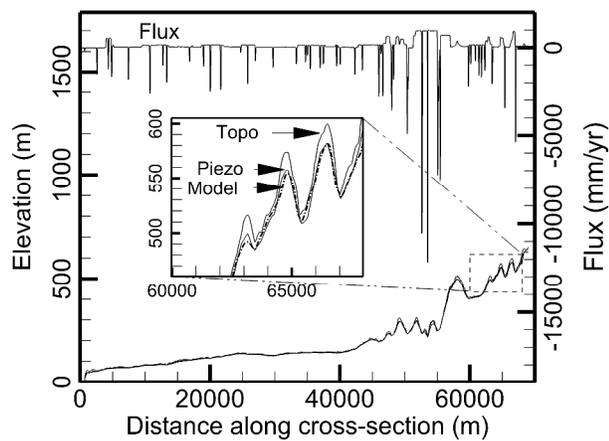
Figure 6. Calibrated recharge fluxes, simulated hydraulic heads, observed water table elevations (from interpolated piezometry) and topographic elevation along the model cross-section. Negative fluxes are exiting the model domain and positive fluxes are entering (corresponding to recharge).

1322x1176mm (96 x 96 DPI)
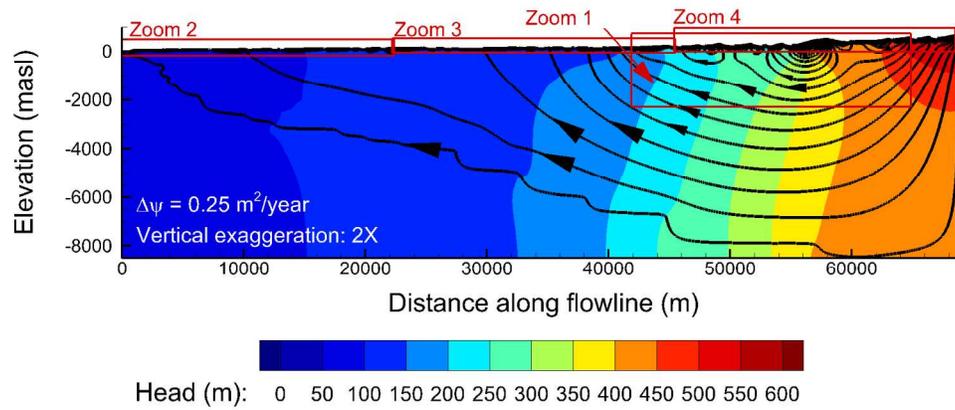
Figure 7. Calibrated steady-state flow model showing hydraulic heads and streamline distribution

529x243mm (96 x 96 DPI)
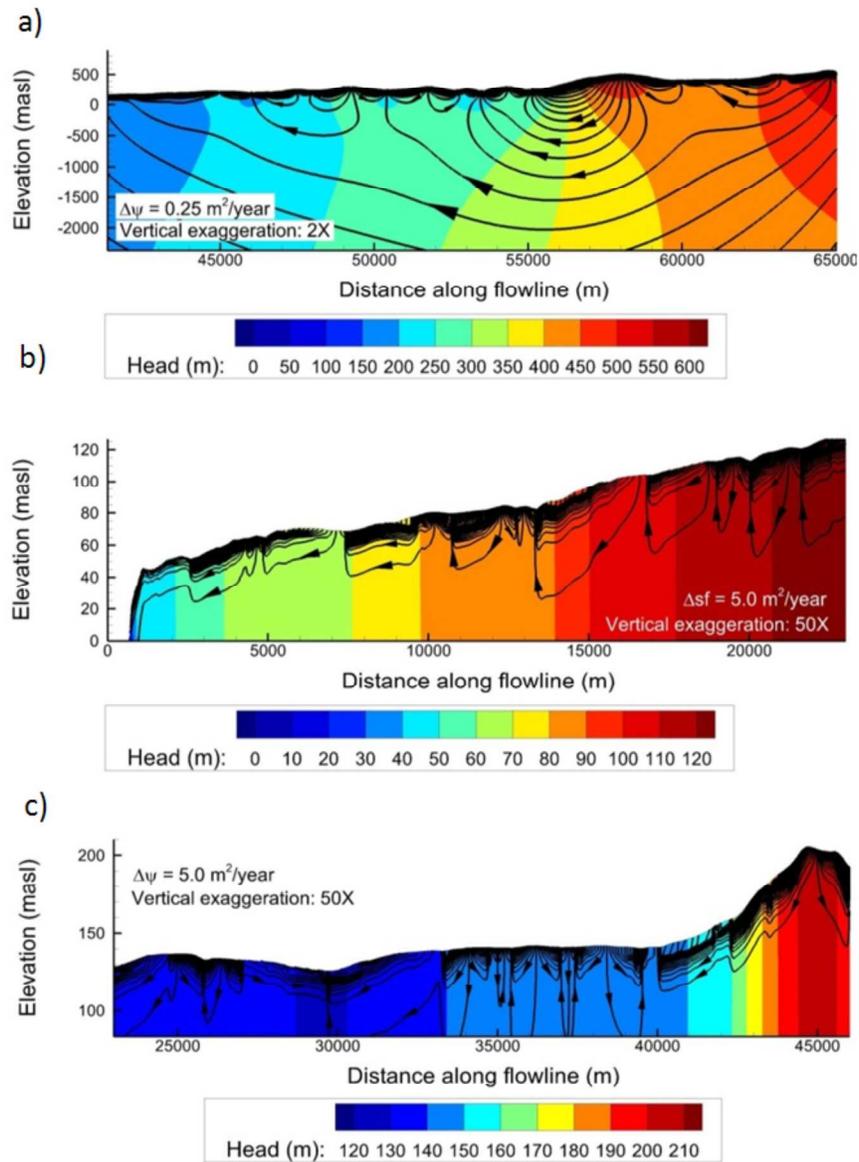
Figure 8. Calibrated flow model a) Zoom 1 (Appalachian Highlands), b) Zoom 2 (St. Lawrence Lowlands close to St. Lawrence River), c) Zoom 3 (St. Lawrence Lowlands close to Appalachian front), showing hydraulic heads and streamline distribution (location shown in Fig. 7).

269x326mm (300 x 300 DPI)
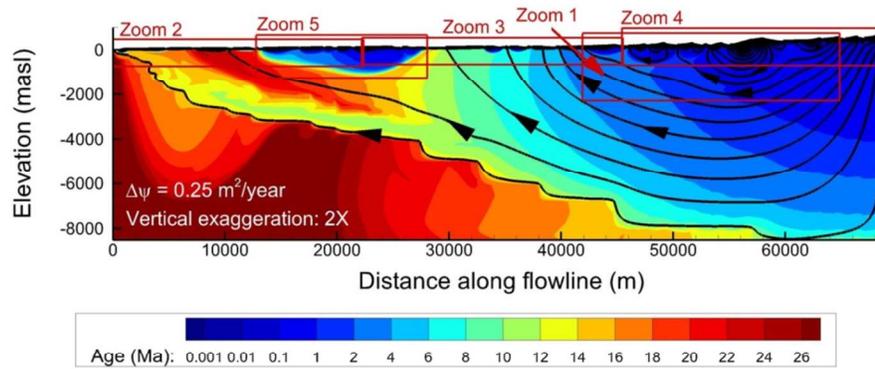
Figure 9. Simulated steady-state mean groundwater ages with superimposed streamlines from the calibrated flow model. (Plot enlargements for Zooms 1, 2 and 4 are provided in Figure 10; Zooms 3 and 5 can be found in Janos, 2013).

449x247mm (300 x 300 DPI)
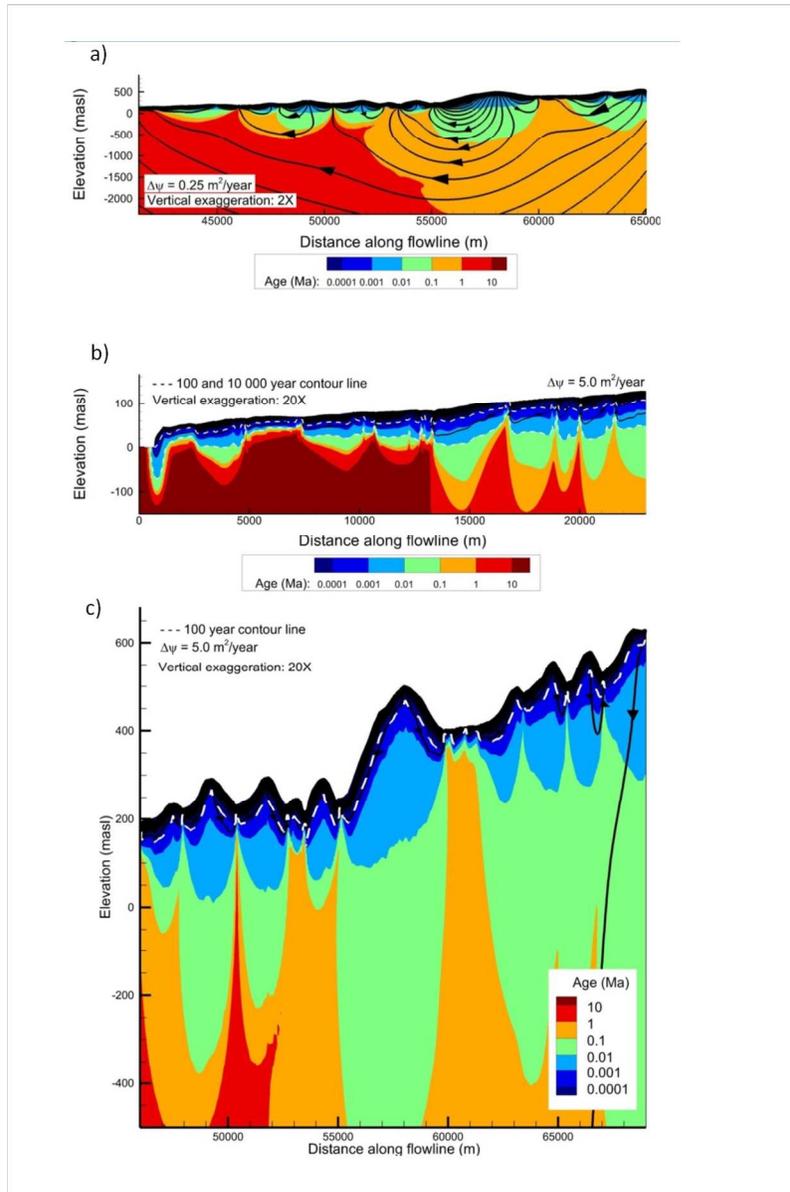
Figure 10 Simulated mean groundwater ages with superimposed streamlines from the calibrated flow model a) Zoom 1, b) Zoom 2, c) Zoom 4. (Locations shown in Fig. 9).

464x696mm (250 x 250 DPI)
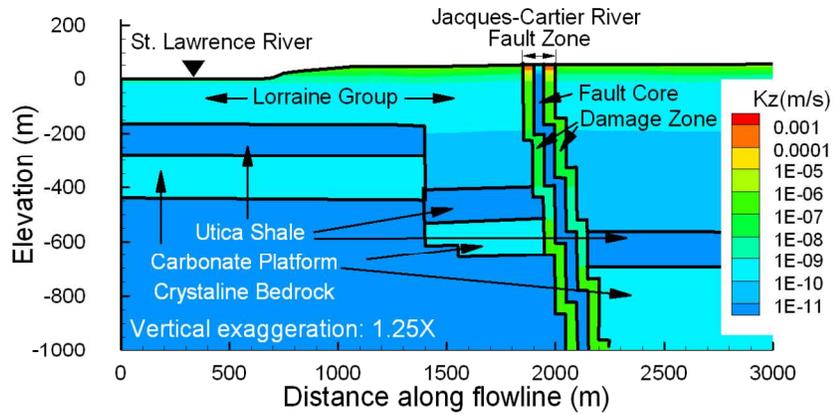
Figure 11 Conceptual model of the Jacques-Cartier River fault zone. Vertical hydraulic conductivities shown correspond to scenario P of the parametric study on faults.

Figure 11 Conceptual model of the Jacques-Cartier River fault zone. Vertical hydraulic conductivities shown correspond to scenario P of the parametric study on faults.

543x316mm (300 x 300 DPI)
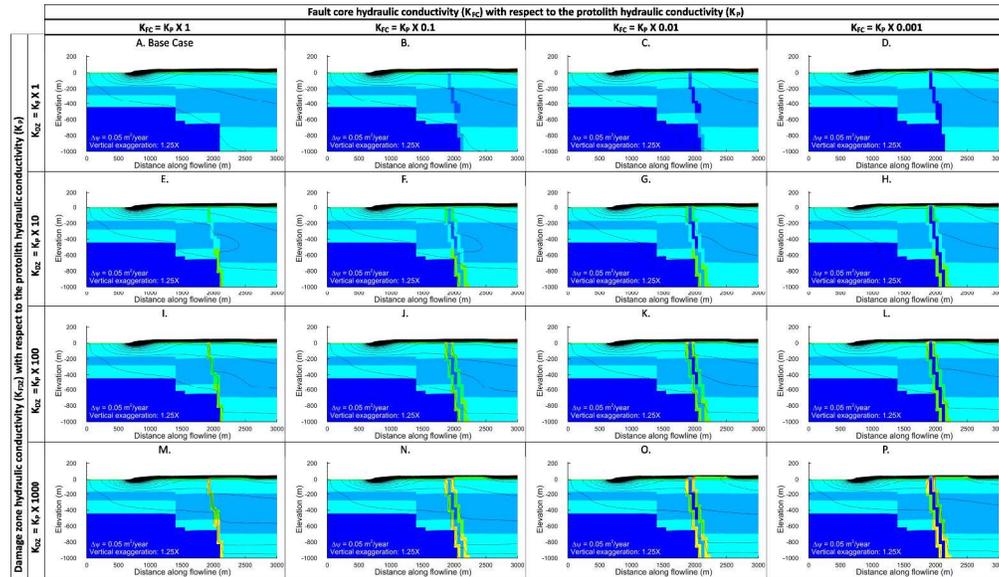
Figure12. Steady-state flow model showing hydraulic conductivities in the horizontal direction and streamlines for fault scenarios described in Table 4, vertical exaggeration is 1.25×.

374x216mm (300 x 300 DPI)

Figure 13. Steady-state flow and age transport model showing mean groundwater and streamlines for fault scenarios described in Table 4, vertical exaggeration is 1.25×.

Figure 13. Steady-state flow and age transport model showing mean groundwater and streamlines for fault scenarios described in Table 4, vertical exaggeration is 1.25×.

381x235mm (300 x 300 DPI)